

An Impact Parameter Dipole Saturation Model

Henri Kowalski

Physics Department, Brookhaven National Laboratory, Upton, NY 11973, USA
Department of Physics, Columbia University, NY 10027, USA
Deutsches Elektronen Synchrotron DESY, Hamburg Germany

Derek Teaney

Physics Department, Brookhaven National Laboratory, Upton, N.Y. 11973, U.S.A.
 (Dated: February 1, 2008)

We develop a dipole model for HERA DIS data which incorporates the impact parameter distribution of the proton. The model describes the inclusive total γ^*p cross-sections as well as the diffractive J/ψ differential cross-sections. We compare the model with previous approaches and show that the t -distributions are sensitive to saturation phenomena. We estimate the boundary of the saturation region and show that it dominates the data in the low- Q^2 region where the total γ^*p cross-section exhibits the same universal rise as hadronic cross-sections. The model is then extended to nuclei and shows good agreement with the nuclear shadowing data at small- x . Finally, we estimate the saturation scale in nuclei.

I. INTRODUCTION

One of the most important observation of the HERA experiments is the rapid rise of the γ^*p cross-section with the γ^*p center of mass energy W in the deep inelastic scattering (DIS) region. This observation indicates that over a region of size $\sim 1/Q^2$ additional gluons are abundantly radiated at small $x \approx Q^2/W^2$. The simultaneous observation of a significant number of diffractive events in DIS lead to the dipole saturation model of Golec-Biernat and Wüsthoff (GBW) [1]. The model successfully described the data in the transition region between low and intermediate Q^2 and indicated the emergence of saturation phenomena in DIS. In spite of its compelling success the model has some obvious shortcomings. First, the treatment of QCD evolution is only rudimentary. Second, the dipole cross-section is integrated over the transverse coordinate although the gluon density is expected to be a strongly varying function of the impact parameter. The evolution was improved by incorporating DGLAP into the dipole cross-section thereby extending the model applicability to the high Q^2 region [2].

In this paper we further improve the dipole model by introducing the impact parameter of the proton into the dipole dynamics. For the form of the dipole cross-section we adopt the Glauber-Mueller formula which can be derived under simplifying assumptions [3]. The transverse profile of the proton can be probed experimentally by measuring the momentum transfer t to the proton in diffractive events. Thus diffractive and inclusive γ^*p processes form a tool to determine the gluon density and saturation dynamics at HERA. Whether the experimental data are sufficient to reveal the rich non-linear dynamics of saturation and the Color Glass Condensate [4] remains an important phenomenological question [5, 6, 7] which this work addresses.

The Impact Parameter (IP) Saturated dipole model can be extended to DIS interactions in nuclei in a natural way. We study nuclear effects and compare them

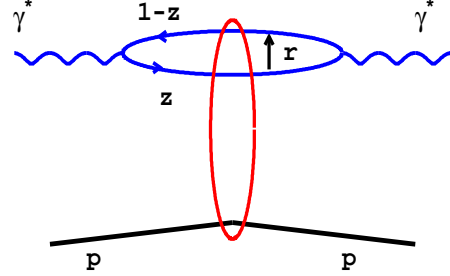


FIG. 1: The interaction of a quark anti-quark dipole with a proton.

with data on nuclear shadowing. Finally we estimate the saturation scale in heavy nuclei.

II. DIPOLE DESCRIPTION OF DIS

In the dipole picture [8, 9], the γ^*p interaction proceeds in three stages: First, the incoming virtual photon fluctuates into a quark-antiquark pair, then the $q\bar{q}$ pair elastically scatters on the proton, and finally the $q\bar{q}$ pair recombines to form a virtual photon. This is shown schematically in Fig. 1. The amplitude for the complete process is simply the product of the amplitudes of these three subprocess. We discuss each in turn.

The amplitude for the incoming virtual photon (with polarization $\lambda = +, -, 0$) to fluctuate into a quark-antiquark pair (of flavor f with helicities $h, \bar{h} = \pm 1/2$) is given by the photon light cone wave-function $(\psi_{\gamma,f})_{\lambda}^{h\bar{h}}$

which depends upon (Q^2, z, \mathbf{r}) . Here z denotes the longitudinal momentum fraction of the photon carried by the quark and \mathbf{r} the transverse size of the $q\bar{q}$ pair. These wave functions are determined from light cone perturbation theory to leading order in the fermion electromagnetic charge [10]. Similarly, the amplitude for the $q\bar{q}$ to recombine to form a virtual photon is $(\psi_{\gamma,f}^*)_{\lambda}^{h\bar{h}}$.

The elastic scattering of the $q\bar{q}$ pair with squared momentum transfer $\Delta^2 = -t$ is described by the elastic scattering amplitude, $A_{el}^{q\bar{q}}(x, r, \Delta)$. (The notation in this section follows S. Munier *et al* [5].) Here A_{el} is defined such that the elastic $q\bar{q}$ cross section is

$$\frac{d\sigma_{q\bar{q}}}{dt} = \frac{1}{16\pi} |A_{el}(x, r, \Delta)|^2. \quad (1)$$

It is convenient to work in coordinate space and define the S-matrix element at a particular impact parameter b

$$S(b) = 1 + \frac{1}{2} \int d^2\Delta e^{i\mathbf{b}\cdot\Delta} A_{el}^{q\bar{q}}(x, r, \Delta). \quad (2)$$

This corresponds to ones intuitive notion of impact parameter only when the dipole size is small compared to the size of the proton. The total cross section for the $q\bar{q}$ pair is found by taking the imaginary part of iA_{el} or in terms of the S-matrix element

$$\sigma_{q\bar{q}}(x, r) = \text{Im } iA_{el}^{q\bar{q}}(x, r, 0) = \int d^2b 2(1 - \text{Re } S(b)). \quad (3)$$

This motivates the definition of the $q\bar{q}$ differential cross section

$$\frac{d\sigma_{q\bar{q}}}{d^2b} = 2(1 - \text{Re } S(b)). \quad (4)$$

The total γ^*p cross section for transverse and longitudinal virtual photons is then given by the imaginary part of the forward scattering amplitude

$$\sigma_{L,T}^{\gamma^*p}(x, Q^2) = \int d^2r \int \frac{dz}{4\pi} \sum_f (\gamma|\gamma)_{L,T}^f \sigma_{q\bar{q}}(x, r), \quad (5)$$

with

$$\sigma_{q\bar{q}}(x, r) = \int d^2b \frac{d\sigma_{q\bar{q}}}{d^2b}. \quad (6)$$

$(\gamma|\gamma)_{L,T}^f$ denotes the probability for a polarized virtual photon to fluctuate into a $q\bar{q}$ pair with flavor f

$$(\gamma|\gamma)_L^f \equiv \sum_{h\bar{h}} (\psi_{\gamma,f}^*)_0^{h\bar{h}} (\psi_{\gamma,f})_0^{h\bar{h}} \quad (7)$$

$$(\gamma|\gamma)_T^f \equiv \frac{1}{2} \sum_{\lambda=\pm 1} (\psi_{\gamma,f}^*)_{\lambda}^{h\bar{h}} (\psi_{\gamma,f})_{\lambda}^{h\bar{h}}. \quad (8)$$

In the dipole picture elastic diffractive vector meson production appears in a similarly transparent way [11].

We denote amplitude for a vector meson to fluctuate into a $q\bar{q}$ pair by $(\psi_V)_{\lambda}^{h\bar{h}}$. This vector-meson wave function will be discussed below. The amplitude for elastic diffractive vector meson production with squared momentum transfer $\Delta^2 = -t$ and transverse (T) or longitudinal polarization (L) is

$$A_{L,T}(\Delta) = \int d^2r \int \frac{dz}{4\pi} \int d^2b (V|\gamma)_{L,T} e^{-i\mathbf{b}\cdot\Delta} 2(1-S(b)). \quad (9)$$

Assuming that the S-matrix element is predominantly real we may substitute $2(1-S(b))$ with $\frac{d^2\sigma_{q\bar{q}}}{d^2b}$. Then, the elastic diffractive cross section is

$$\frac{d\sigma_{L,T}}{dt} = \frac{1}{16\pi} \left| \int d^2\mathbf{r} \int \frac{dz}{4\pi} \int d^2b (V|\gamma)_{L,T} e^{-i\mathbf{b}\cdot\Delta} \frac{d\sigma_{q\bar{q}}}{d^2b} \right|^2. \quad (10)$$

Note, it is the total dipole cross section at a particular impact parameter which appears in this formula. S. Munier *et al* [5] extracted $S(b)$ from the diffractive data using the formalism outlined above.

III. MODEL DESCRIPTION

In order to describe the data it is necessary to make specific assumptions about the dipole cross section and the photon and vector meson wave-functions. First, we give a simple model for the dipole cross section and contrast this model with other models that have appeared previously. Then we define the gluon structure function $xg(x, \mu^2)$ and the proton shape function $T(b)$ which enters the dipole cross-section. Then we define and discuss the properties of the vector meson wave-functions in some detail. Finally after the dipole cross-section and the wave-functions are specified, we determine the model parameters by fitting the inclusive total cross section and elastic diffractive vector meson data.

A. The Dipole Cross Section

The total cross section for a small $q\bar{q}$ dipole to pass through a dilute gluon cloud is proportional to the dipole area, the strong coupling constant, and the number of gluons in the cloud [12]

$$\sigma_{q\bar{q}} = \frac{\pi^2}{N_c} r^2 \alpha_s(\mu^2) xg(x, \mu^2), \quad (11)$$

where $xg(x, \mu^2)$ is gluon density at some scale μ^2 . Now imagine that the density of gluons in the target is not small. Divide the target into thin slices of thickness dz [46]. The probability that a dipole at impact parameter b does not suffer an inelastic interaction passing through one slice of the proton is

$$P(b) = 1 - \frac{\pi^2}{N_c} r^2 \alpha_s(\mu^2) xg(x, \mu^2) \rho(b, z) dz. \quad (12)$$

Here $\rho(b, z)$ denotes density of the gluons within a proton and is normalized to one

$$\int d^2b dz \rho(b, z) = 1. \quad (13)$$

Exponentiating this result, the probability that the dipole suffers no inelastic interactions passing through the entire proton is $|S(b)|^2$

$$|S(b)|^2 = \exp\left(-\frac{\pi^2}{N_c} r^2 \alpha_s(\mu^2) xg(x, \mu^2) T(b)\right). \quad (14)$$

Here $T(b)$ is the thickness function,

$$T(b) = \int_{-\infty}^{\infty} dz \rho(b, z). \quad (15)$$

To obtain the total cross section at a given impact parameter we assume that the S-matrix element is predominantly real. Then the cross section at a given impact parameter b is given by $2(1 - \text{Re}S(b))$ or

$$\frac{d\sigma_{q\bar{q}}}{d^2b} = 2 \left[1 - \exp\left(-\frac{\pi^2}{2N_c} r^2 \alpha_s(\mu^2) xg(x, \mu^2) T(b)\right) \right]. \quad (16)$$

This expression is known as the Glauber-Mueller dipole cross section [3] and can also be obtained within the McLerran-Venugopalan model [13]. It provides a simple model for the interaction of a $q\bar{q}$ probe with a dense target. The function $T(b)$ and $xg(x, \mu^2)$ are determined from the fits to the data. Figure 2 shows the dipole cross section as a function of the impact parameter b for various dipole sizes at two distinct x -values. The properties of the dipole cross-section will be discussed below. Similar dipole cross sections were found in the model of Ref. [14]. The cross-section is evaluated for the largest dipole sizes only to illustrate saturation in the Glauber-Mueller approach. This dipole size is not contributing to the observed cross-section.

The Glauber-Mueller dipole cross section is a simple model which respects unitarity. As discussed below, in the large Q^2 region the model matches smoothly onto DGLAP since we will evolve $xg(x, \mu^2)$ with DGLAP. In the small x region, the model evolution can be improved. Indeed, evolution based upon the Balitsky-Kochegov equation [15, 16] has been extensively studied [6, 7] and provides a reasonable description of the total and total diffractive cross sections. Nevertheless, the Glauber-Mueller dipole cross section provides a simple model which exhibits saturation as a function of impact parameter in a reasonably generic way and is therefore a useful tool in exposing saturation effects in the data.

B. The Proton Shape $T(b)$

The impact parameter dependence of the dipole cross-section determines the properties of the t -distributions

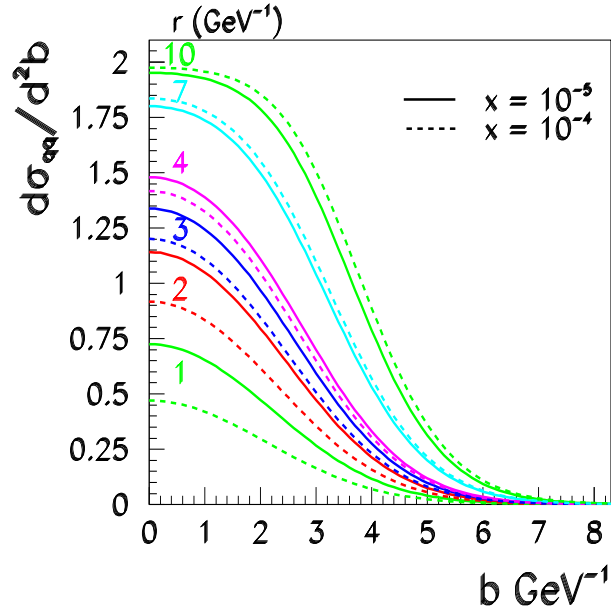


FIG. 2: The dipole cross-section as a function of the impact parameter b for various dipole sizes evaluated at two x -values.

in elastic diffractive processes. Here the variable t denotes the squared four momentum transfer between the incoming and outgoing proton in the diffractive process, $\gamma^*p \rightarrow Vp$. The t -distribution is directly related to the Fourier transform of $T(b)$ via Eqs. 16 and 10. Presently, the best data on diffractive t -distributions are available for vector-meson production. HERA experiments reported [17, 18, 19] that all diffractive vector-meson t -distributions can be described by a single exponent B for $|t| < 1 \text{ GeV}^2$

$$\frac{d\sigma_{VM}^{\gamma^*p}}{dt} \propto \exp(-B|t|). \quad (17)$$

Since the J/ψ wave-function is better known than the ρ or ϕ wave-functions, we will concentrate on J/ψ production. The value of the coefficient B for the J/ψ t -distribution is around 4 GeV^{-2} and is only weakly dependent W^2 and Q^2 . The exponential form in Eq. 17 is the Fourier transform of

$$T_G(b) = \frac{1}{2\pi B_G} \exp(-b^2/2B_G). \quad (18)$$

We therefore tried this form for $T(b)$. To account for the expected exponential behavior at large impact parameters we also considered the form

$$T_{GY}(b) \propto \int d^2b' \exp(-(\mathbf{b} - \mathbf{b}')^2/2B_{GY}) K_0(b'/W_{GY}). \quad (19)$$

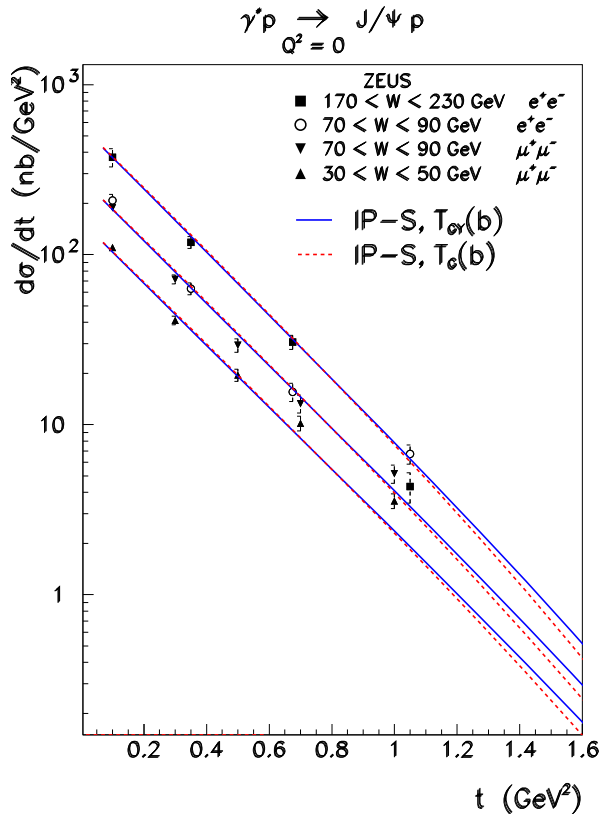


FIG. 3: The differential cross-section for exclusive diffractive J/ψ production as a function of t for representative bins in W [19]. The solid (dashed) lines show the results of the IP saturation model assuming T_{GY} (T_G) for the proton shape.

Due to the asymptotic behavior of $K_0(x) \sim \sqrt{\pi/2x} \exp(-x)$, $T_{GY}(b)$ falls off exponentially at large impact parameters.

The parameters B_G , B_{GY} and W_{GY} are only weakly dependent on the other parameters in the model and were determined iteratively. From the fit to the limited t range, $|t| < 0.7 \text{ GeV}^2$, the following values were found: $B_G = 4.25 \text{ GeV}^{-2}$ for $T_G(b)$ and $B_{GY} = 3.25 \text{ GeV}^{-2}$ and $W_{GY} = 0.66 \text{ GeV}^{-1}$ for $T_{GY}(b)$. Figure 3 shows a representative subset of data [19] together with the results of a fit to the data using both forms of $T(b)$. The slope of the data fixes the parameters B_G and B_{GY} and W_{GY} . The normalization of the curves in Figure 3 is a determined by the underlying J/ψ light cone wave function and is therefore model dependent. We will use three model wavefunctions which are discussed more fully in Sect. III F and in the Appendix. The figure is for the CORNELL wavefunction. Unless explicitly stated, the profile function adopted throughout the rest of this work is $T_{GY}(b)$ which for practical purposes is equivalent to $T_G(b)$.

C. Gluon Structure Function and Dipole Evolution

The dipole cross-section (Eq. 16) requires the gluon density $xg(x, \mu^2)$ for all scales μ^2 . As in previous work [2], the scale μ^2 is related to the dipole size by

$$\mu^2 = \frac{C}{r^2} + \mu_0^2. \quad (20)$$

The gluon density is evolved to the scale μ^2 with leading order DGLAP without quarks for the gluon density. The evolution of the gluon density is performed numerically for every dipole size r during the integration of Eq. 5. The initial gluon distribution is taken at the scale μ_0^2 in the form

$$xg(x, \mu_0^2) = A_g x^{-\lambda_g} (1-x)^{5.6}. \quad (21)$$

The parameters of the model C , μ_0^2 , A_g , and λ_g are determined from a fit to the DIS data. For light quarks the gluon distribution is evaluated at $x = x_{BJ} = \frac{Q^2}{Q^2 + W^2}$. For the charm quark the gluon structure function is evaluated at $x = (4m_c^2 + Q^2)/(Q^2 + W^2)$, where m_c is the charm quark mass [20]. This implies that the dipole cross section is flavor dependent when performing the sum over flavors in Eq. 5.

The present model has, in some sense, one less parameter than the model of Ref. [2]. The parameter σ_0 which previously determined the asymptotic size of the dipole cross-section is now replaced by the parameter B_G (or B_{GY} and W_{GY}) which is (are) fixed by the shape of the diffractive t -distribution.

The gluon structure function obtained from the fit is shown in Fig. 4 for various dipole sizes. The dipole size determines the evolution scale μ^2 through Eq. 20. QCD evolution changes the rate of rise of the gluon structure function $xg(x, \mu^2)$. The rate of rise is usually quantified by the exponent λ_{eff} ,

$$\lambda_{eff} = \frac{d \log(xg(x, \mu^2))}{d \log(1/x)}. \quad (22)$$

The exponent λ_{eff} is a measure of the strength of gluon emission process, see e.g. [22]. Figure 5 shows a rapid increase of the exponent λ_{eff} with decreasing x for small values of the dipole radius r .

D. Comparison with the GBW model

In the original GBW model [1] the dipole cross section $\sigma_{q\bar{q}}(x, r)$ was independent of impact parameter and gave a good description of the inclusive total γ^*p cross section. It also described some diffractive processes [1, 2, 23] without providing any information about the t -dependence. In the GBW model the dipole cross-section σ_{qq} is given by

$$\sigma_{q\bar{q}}^{GBW} = \sigma_0 \left[1 - \exp\left(-\frac{r^2}{R_0^2}\right) \right], \quad (23)$$

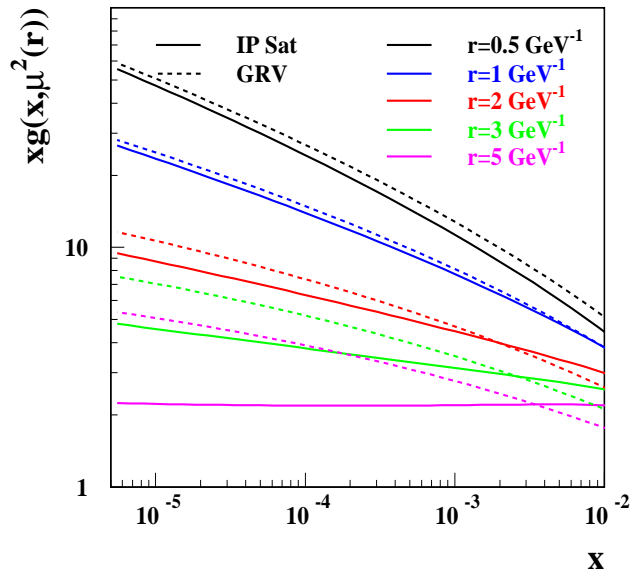


FIG. 4: The gluon structure function for various dipole sizes. The dipole size determines the evolution scale μ^2 . The dashed lines show the GRV results [21].

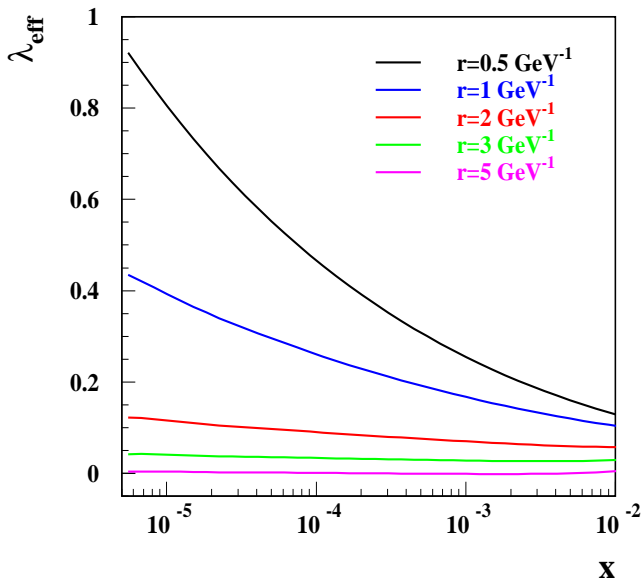


FIG. 5: The logarithmic rate of rise of the gluon structure function as a function x , $\lambda_{eff} = \frac{d \log(xg(x, \mu^2))}{d \log(1/x)}$. λ_{eff} is a measure of the strength of the gluon emission process.

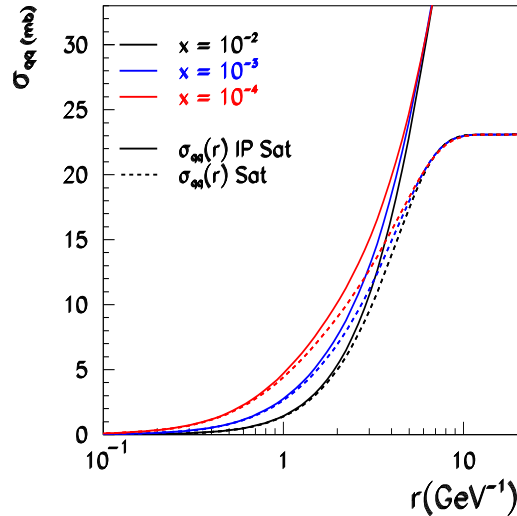


FIG. 6: The integrated dipole cross section as a function of the dipole size. The solid and dashed curves trace the dipole cross-section in the IP Saturation model and the saturation model of Ref. [2] respectively.

where R_0 denotes the saturation radius and σ_0 is a constant. The saturation radius is x dependent

$$R_0^2 = \frac{1}{\text{GeV}^2} \left(\frac{x}{x_0} \right)^{\lambda_{GBW}}. \quad (24)$$

The parameters $\sigma_0 = 23$ mb, $\lambda_{GBW} = 0.29$ and $x_0 = 3 \cdot 10^{-4}$ were determined from a fit to the data. The saturation radius R_0 is analogous to the gluon distribution and determines the growth of the total and diffractive cross sections with decreasing x . For large size dipoles σ_{qq}^{GBW} saturates by approaching a constant value σ_0 which is independent of the exponent λ_{GBW} .

Once the impact parameter is included saturation becomes b dependent. For small values of b , the cross-section grows rapidly with r until it reaches the saturation plateau seen in Fig. 2, $d\sigma_{qq}/d^2b = 2$. The extension of the plateau b_S can be estimated from the condition $\frac{\pi^2}{2N_C} r^2 \alpha_s(\mu^2) xg(x, \mu^2) T(b_S) = 1$. Using the Gaussian form of $T(b)$ and approximating $xg(x, \mu^2) \sim (x_0/x)^{\lambda_{eff}}$ we obtain

$$b_S^2 = 2B_G \log \left(\frac{\pi}{4N_C B_G} r^2 \alpha_s(\mu^2) (x_0/x)^{\lambda_{eff}} \right). \quad (25)$$

Thus, the integrated dipole cross-section σ_{qq} increases logarithmically for large r and small x due to the growth of the plateau region. The logarithmic growth of the cross-section at small x is determined by λ_{eff} and B_G . This behavior should be compared to the GBW cross section which becomes a constant σ_0 that is independent of λ_{GBW} . The differences are illustrated in Fig. 6.

E. Photon wave-function

The longitudinal and transverse photon wave-function in the conventions of Ref. [24] are given by

$$\begin{aligned}
(\psi_{\gamma,f})_0^{h\bar{h}}(r,z) &= e_f \delta_{f\bar{f}} \sqrt{N_c} [-2z(1-z)Q(\delta_{h+\bar{h}-} + \delta_{h-\bar{h}+})] \frac{K_0(\epsilon r)}{2\pi} \\
(\psi_{\gamma,f})_{+1}^{h\bar{h}}(r,z) &= e_f \delta_{f\bar{f}} \sqrt{2N_c} [-ie^{+i\varphi r} (z\delta_{h+\bar{h}-} - (1-z)\delta_{h-\bar{h}+}) \partial_r + m_f \delta_{h+\bar{h}+}] \frac{K_0(\epsilon r)}{2\pi} \\
(\psi_{\gamma,f})_{-1}^{h\bar{h}}(r,z) &= e_f \delta_{f\bar{f}} \sqrt{2N_c} [+ie^{-i\varphi r} ((1-z)\delta_{h+\bar{h}-} - z\delta_{h-\bar{h}+}) \partial_r + m_f \delta_{h-\bar{h}-}] \frac{K_0(\epsilon r)}{2\pi}
\end{aligned} \tag{26}$$

where $re^{i\varphi r} = r_x + ir_y$, $\epsilon^2 = z(1-z)Q^2 + m_f^2$, e_f is the electromagnetic charge of quark flavor f , and $\partial_r K_0(\epsilon r) = -\epsilon K_1(\epsilon r)$.

For small dipoles ($\epsilon r \ll 1$) the photon wave-function scales as $K_1(\epsilon r) \sim 1/\epsilon r$. For large dipoles ($\epsilon r \gg 1$), the wave-function falls off exponentially with the quark mass, $K_1(\epsilon r) \sim \sqrt{\pi/2\epsilon r} \exp(-\epsilon r)$.

F. Vector Meson Wave-Function

To describe vector meson production, we developed several models of the J/ψ light cone wave-function, $(\psi_V)_\lambda^{h\bar{h}}$. These phenomenological wave-functions should satisfy several model independent constraints [25, 26]. First, the wave-function must satisfy the normalization condition

$$1 = \int \frac{d^2k dz}{16\pi^3} \sum_{h\bar{h}} |(\tilde{\psi}_V)_\lambda^{h\bar{h}}(k,z)|^2. \tag{27}$$

Second, the decay width of the vector meson further constrains the wave-function. Precise definitions and explicit formulas for the decay width and other constraints on the longitudinal and transverse wave functions are given in the Appendix.

As an example, we model the J/ψ wave-function as a Gaussian in momentum space in the meson rest frame

$$\tilde{\psi}_{NR}(p) = N_{L,T} \exp\left(-\frac{p^2}{\omega_{L,T}^2}\right), \tag{28}$$

where \vec{p} denotes the charmed quark 3-momentum. In DIS reactions the meson wave-functions are defined on the light-cone and not in the J/ψ rest frame. Following Frankfurt and Strikman [25] we boost the J/ψ wave-function from the rest frame to the light-cone. The constants $N_{L,T}$ and $\omega_{L,T}$ were adjusted to satisfy the normalization and decay constraints. This wave-function is denoted Gaus-RF (Rest Frame).

As noted in Ref. [25] this procedure does not lead to the proper asymptotic form of the light cone wave function

at small distances, $\tilde{\phi} \sim z(1-z)$. Therefore, we also considered a Gaussian wave-function defined directly on the light cone

$$\tilde{\phi}_{L,T}(k,z) = N_L z(1-z) \exp\left(-\frac{k^2}{\omega_L^2}\right). \tag{29}$$

Once again, the norm and decay width constrain N_L and ω_L . This wave-function is denoted Gaus-LC (Light Cone).

J/ψ wave-functions were also studied with potential models [27, 28, 29] and successfully describe the energy levels of $c\bar{c}$ bound states. Potential models were less successful at reproducing the meson decay width which is sensitive to the short distance behavior of the wave-function. This shortcoming may be less important since the short distance behavior of the wave-function is suppressed by the vanishing dipole cross section at small r . We determined the non-relativistic wave-function by integrating the radial Schrödinger equation with the Cornell potential [27]. As before we naively boosted this wave-function to the light-cone. Naturally, this wave-function is denoted CORNELL.

In order to visualize the meson wave-function we define the meson photon overlap $p_{\gamma^*V}(r)$ as

$$p_{\gamma^*V}(r) = r \int \frac{dz}{4\pi} (\gamma|V)_T, \tag{30}$$

which has the simple interpretation as the amplitude for diffractive vector meson production from the elastic scattering of a dipole of radius r . The overlap function is shown in Fig. 7 for the transverse component of the three J/ψ wave-functions considered in the paper.

G. Dipole size

To interpret the IP Saturation model physically, we determined the typical dipole size contributing to the total cross-section. The distribution of dipole sizes $\frac{1}{\sigma^{\gamma^*p}} \frac{d\sigma^{\gamma^*p}}{dr}$

is the integrand of Eq. 5 after the z integration is performed. Figure 8 shows this distribution at representative values of x and Q^2 . For each illustrated x and Q^2 the arrow indicates the median radius of a dipole which scatters off the proton. Note that at smallest Q^2 and $x = 10^{-5}$ the majority of dipoles are smaller than $r \lesssim 2 \text{ GeV}^{-1}$ and thus half of the dipoles are perturbative.

IV. RESULTS FOR γ^*p PROCESSES

A. Inclusive total cross-section

The fit to the total γ^*p cross-section data was performed in the range $x < 0.01$ and $Q^2 > 0.25 \text{ GeV}^2$. The small x cut leads to an upper limit on Q^2 , $Q^2 < 200 \text{ GeV}^2$. Figure 9 shows the γ^*p cross section as a function of W^2 at the various Q^2 measured by the HERA experiments [30]. Following the rise of the total cross section with W^2 at fixed Q^2 , we observe a striking change: for small Q^2 (the top of Fig. 9) the cross section rises slowly with the center of mass energy W^2 , while for large Q^2 (the bottom of Fig. 9) the cross section rises strongly. If we parameterize the cross section by a power law

$$\sigma_{tot}^{\gamma^*p} \sim (W^2)^{\lambda_{tot}(Q^2)} \sim (1/x)^{\lambda_{tot}(Q^2)}, \quad (31)$$

this change in the rate of rise from low to high Q^2 translates into a Q^2 dependence of the exponent λ_{tot} . $\lambda_{tot}(Q^2)$ is illustrated in Fig. 10 and summarizes one of the principle observations at HERA. At small Q^2 , σ_{γ^*p} increases

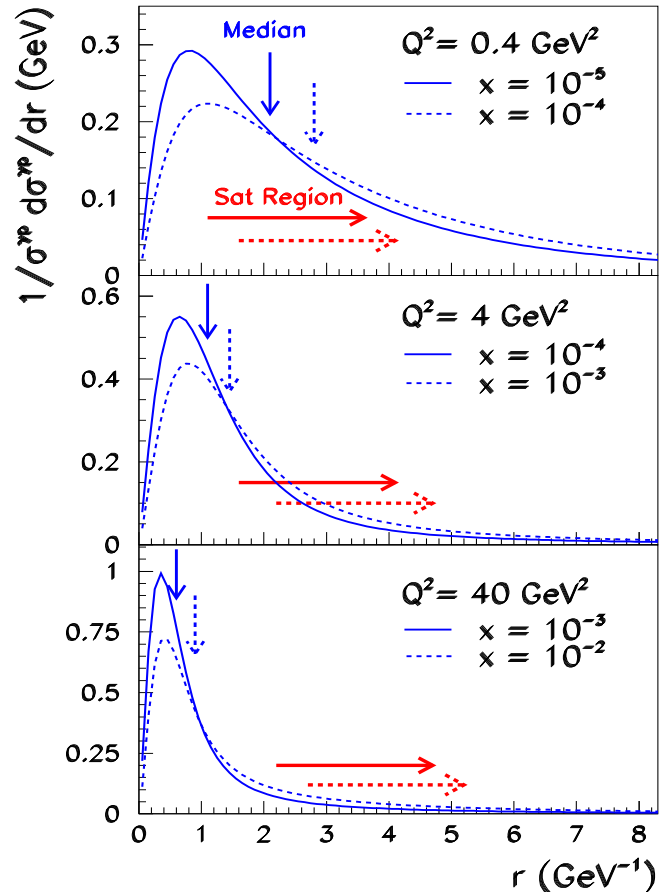


FIG. 8: The distribution of the dipole sizes contributing to the inclusive total cross-section at various virtualities Q^2 and some representative x values. The vertical arrows indicate the median radius of a dipole which scatters off the proton. The horizontal arrows indicate saturation region $r > r_s(b, x)$ at $b = 0$. See Table II.

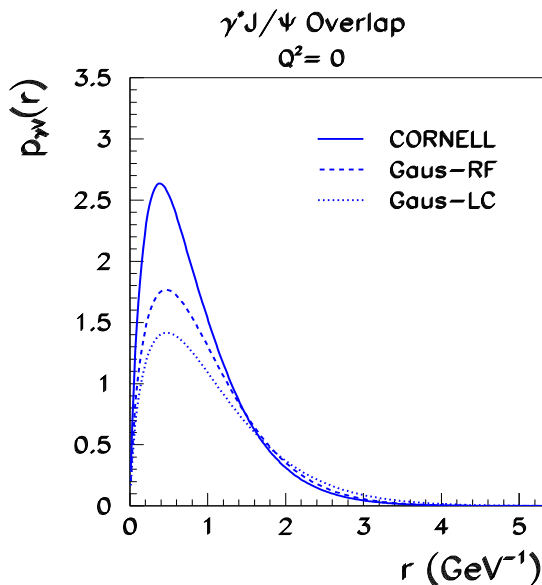


FIG. 7: A comparison of the meson photon overlap function (Eq. 30) for the three different J/ψ wave-functions adopted in this work.

with W^2 as in all hadronic reactions, $\lambda_{tot} \approx 0.08$ [31]. At large Q^2 the exponent λ_{tot} increases substantially.

In the IP Saturation model the increase of the exponent λ_{tot} with Q^2 is a consequence of the DGLAP evolution. When the dipole size becomes smaller than $\sim \frac{2}{\mu_0}$ DGLAP evolution becomes increasingly effective and the growth of the gluon distribution at small x becomes increasingly rapid. Mathematically speaking, λ_{eff} increases for small size dipoles as seen in Fig. 5. Averaging over dipole sizes with the photon wave function translates $\lambda_{eff}(r)$ into $\lambda_{tot}(Q^2)$. The large increase in λ_{tot} with Q^2 indicates a transition from a predominance of large to a predominance of small dipoles when evaluating the cross-section. The contribution of large dipoles at low Q^2 is determined by the light quark mass, $m_{u,d,s}$.

The parameters A_g , λ_g and μ_0^2 were found by fitting

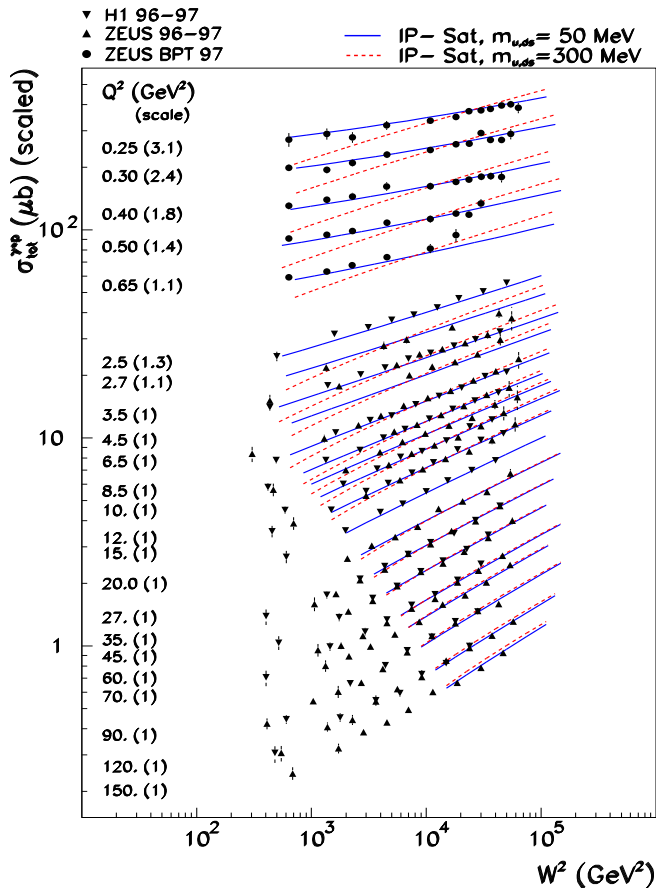


FIG. 9: The γ^*p cross section as a function of W^2 at various Q^2 . The values of Q^2 are shown on the left side of the plot along with the scale factor applied to the data for a better visibility. The full (dashed) line shows a fit by the IP Saturation Model with $m_{u,d,s} = 50$ MeV ($m_{u,d,s} = 300$ MeV). The fits are performed for $x < 0.01$.

$m_{u,d,s}$ (MeV)	A_g	λ_g	μ_0^2	χ^2/N_{DF}
300	1.67	0.226	6.85	702/160
150	2.34	0.043	1.32	199/160
100	2.85	-0.04	0.96	153/160
50	3.47	-0.12	0.77	137/160

TABLE I: Table of parameters determined in the fit to the total γ^*p cross-section for different assumptions on the light quark mass $m_{u,d,s}$.

the total γ^*p cross-section for various light quark masses. The parameter C is strongly correlated to the parameters A_g and λ_g and does not affect the fit quality. Therefore, we set $C = 4$ by fiat. The mass of the charm quark was $m_c = 1.3$ GeV as required by elastic diffractive J/ψ production discussed below. The results of the fits to the ZEUS data are collected in Table I. Because of the good agreement between the H1 and ZEUS data sets the com-

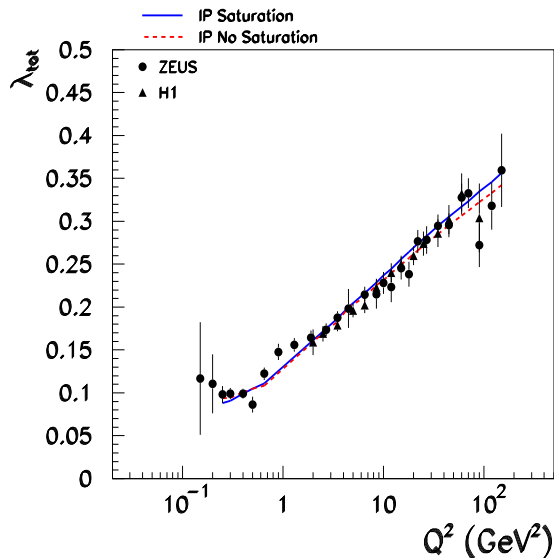


FIG. 10: The exponent λ_{tot} as a function of Q^2 . λ_{tot} parametrizes the total cross section at fixed Q^2 , $\sigma_{tot}^{\gamma^*p} \sim (1/x)^{\lambda_{tot}}$.

pared H1-ZEUS fit returns nearly identical parameters. The fits show a clear preference for the light quark mass of $m_{u,d,s} = 50$ MeV, which is taken as a reference value. Note, the quality of the fit reported here is even better than the fits of Ref. [2].

As seen in Table I, when light quark mass is increased, the fit subsequently increases λ_g . DGLAP evolution can only increase the observed rate of rise of the cross section with W^2 , $\lambda_{tot} > \lambda_g$. Therefore, as seen in Fig. 9, for larger masses of the light quarks the cross section rises too quickly with W^2 at low Q^2 . It is certainly known that the strange quark mass is heavier than the u and d quarks. However, the influence of the strange quark on the overall fit is relatively small since its contribution to F_2 is suppressed relative to the u, d contribution by the ratio of charges squared, $e_s^2/(e_u^2 + e_d^2) = 1/5$. Therefore, we have neglected the difference between the s and u, d quark masses. Including a heavier strange quark would make the fit only marginally worse. However, the clear dependence of the fit quality on the mass of the light quark is a property of the model. It is due to the interplay of DGLAP evolution and the properties of the photon wave function. It may indicate the shortcomings of the wave function at large distances.

In contrast to the GBW model [1] and the model of Ref. [2], saturation is not responsible for the change in λ_{tot} with Q^2 once the impact parameter is included. This is because the total dipole cross section continues to grow within the saturation region although the differential dipole cross-section has attained its asymptotic value $\frac{d\sigma}{d^2b} = 2$. Therefore, for the total cross-section saturation

effects are smaller than in the original GBW model. However, for diffractive t -distributions saturation will appear more clearly.

B. Charm Production

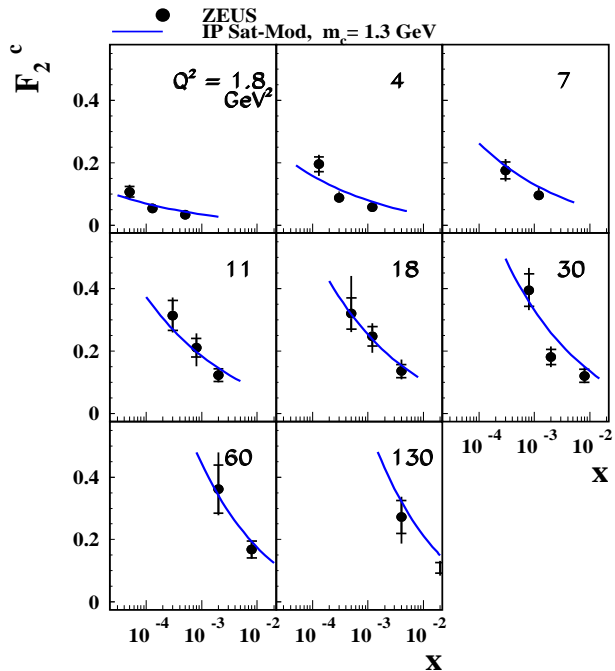


FIG. 11: A comparison of the measured F_2^c [32] to the results of the model.

The dipole model makes a direct prediction for the inclusive charm contribution to F_2 . In the dipole approach the charm quark distribution is calculated from the gluon distribution. Figure 11 shows a comparison between the measured and predicted values of the charm structure function F_2^c . The results depend weakly on the charm mass. The good agreement with data for both ZEUS and H1 experiments [32, 33] confirms the consistency of the model and supports the dipole picture.

C. Determination of F_L

As a byproduct of our investigation we determined the longitudinal structure function F_L . A measurement of F_L would be a critical test of our understanding of the gluon distribution. F_L is zero in the naive parton model and is non-zero only after gluon radiation is included. In dipole models at small x , both F_L and F_2 are governed by the gluon distribution and therefore they behave simi-

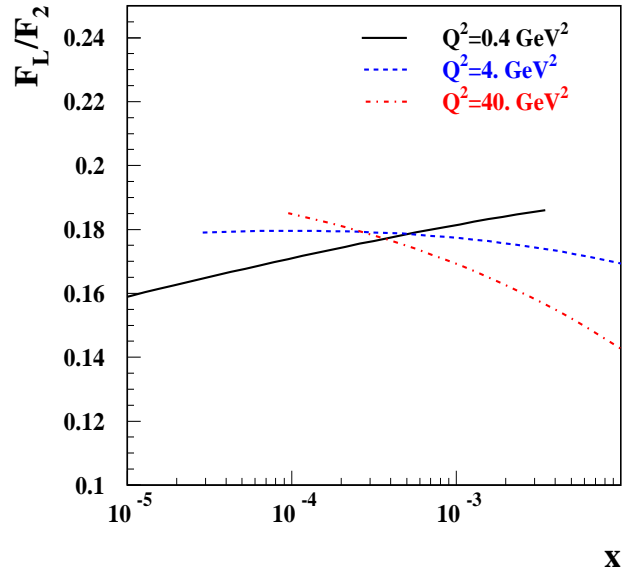


FIG. 12: The ratio F_L/F_2 as a function of x at various photon virtualities.

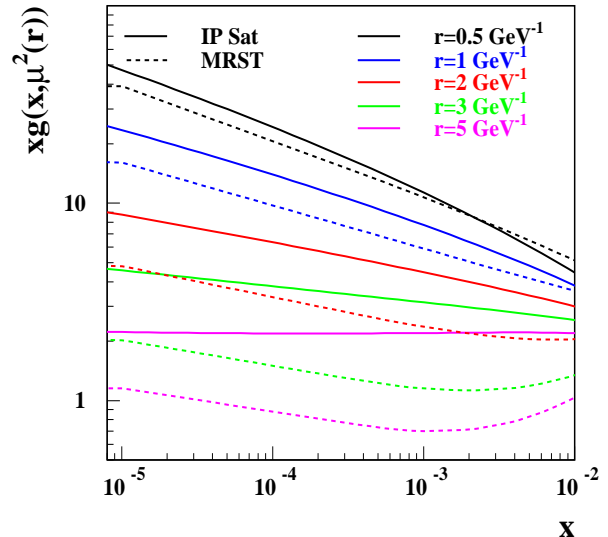


FIG. 13: A comparison of the gluon structure function of the IP Saturation model with the results of the MRST fit [34] for various dipole sizes. The dipole size determines the evolution scale μ^2 .

larly. Figure 12 shows the ratio of F_L to F_2 as a function of x for various photon virtualities. The ratio is around 18 % and gently varies with x . In the standard QCD fits F_L/F_2 may show a stronger variation with x at low Q^2 [35]. This is because the shape of the gluon structure function seen in Fig. 13 is very different from the dipole model presented here. The difference in the gluon structure function between the MRST fit [34] and the dipole model fit is due to the sea quark contribution. In the MRST fit the initial sea quark contribution is independent of the gluon distribution and subsequently influences the gluon evolution. In the dipole fit the sea quark distribution is always derived from the gluon distribution. It is important to measure F_L in order to determine the gluon density precisely and to clarify the relative roles of gluons and sea quarks.

D. J/ψ production

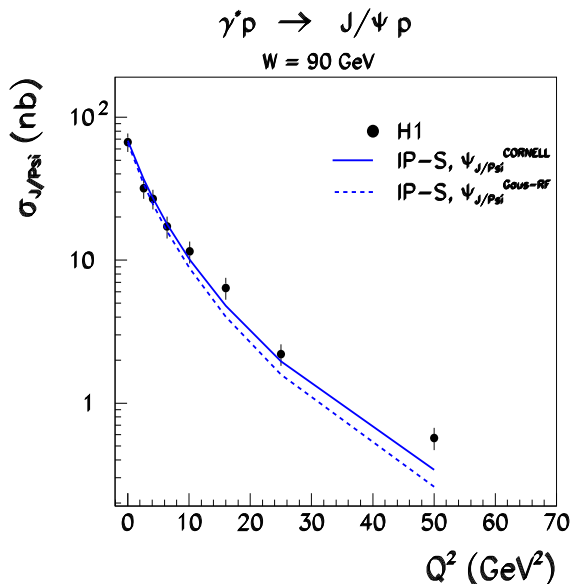


FIG. 14: A comparison of the measured total elastic diffractive J/ψ cross-sections [18] with the results of the model.

The cross sections for elastic diffractive J/ψ production were calculated using Eq. 10 with the dipole cross section determined by fitting σ_{γ^*p} . Figure 14 compares the computed total J/ψ cross-section with H1 measurements [18] for various photon virtualities at $W = 90$ GeV. The absolute magnitude of the cross-sections is very sensitive to the charm quark mass. The charm quark mass was adjusted to $m_c = 1.3$ GeV in order to match the experimental cross section at $Q^2 = 0$. A small shift of 50 MeV in the charm mass changes the cross-section by around 15%.

The predicted total J/ψ cross-sections for the Gaus-

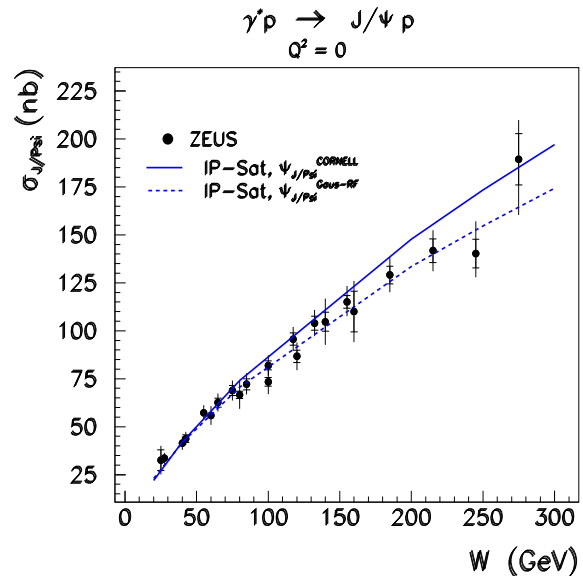


FIG. 15: A comparison of the measured total elastic diffractive J/ψ cross-sections [19] with the results of the model.

RF and Gaus-LC wave-functions are very similar in the Q^2 range considered. Therefore, we only show the predictions of the Gaus-RF wave-function in what follows. The CORNELL wave-function, which is more concentrated at the origin leads to a prediction which is in significantly better agreement with data at large Q^2 , see Fig. 14. In contrast to Ref. [25], the scale $\mu^2 = C/r^2 + \mu_0^2$ is fixed with $C = 4$. Within the range $C = 1 \sim 10$ the results were almost independent of the parameter C after refitting total γ^*p cross-section.

Figure 15 compares model predictions with the measured J/ψ cross-section as a function of energy W at $Q^2 = 0$. In this case, both J/ψ wave-functions are in good agreement with the data.

Note, there is a $\sim 15\%$ discrepancy in the normalization of the J/ψ cross-sections between ZEUS and H1. This discrepancy was absorbed in the charm quark mass; we take $m_c = 1.25$ GeV when comparing with ZEUS data and $m_c = 1.3$ GeV when comparing with H1.

E. t distributions for J/ψ production

Figure 16 compares the J/ψ diffractive cross-section as a function of t for various W^2 to model predictions. In the measured region, both J/ψ wave-functions lead to very similar results although at large t they start to differ significantly. In the large t region the exponential behavior of the differential cross section is considerably distorted and the IP Saturation model predicts diffractive dips. Figure 17 illustrates the emergence of the dip by displaying the Fourier transform of the differential dipole

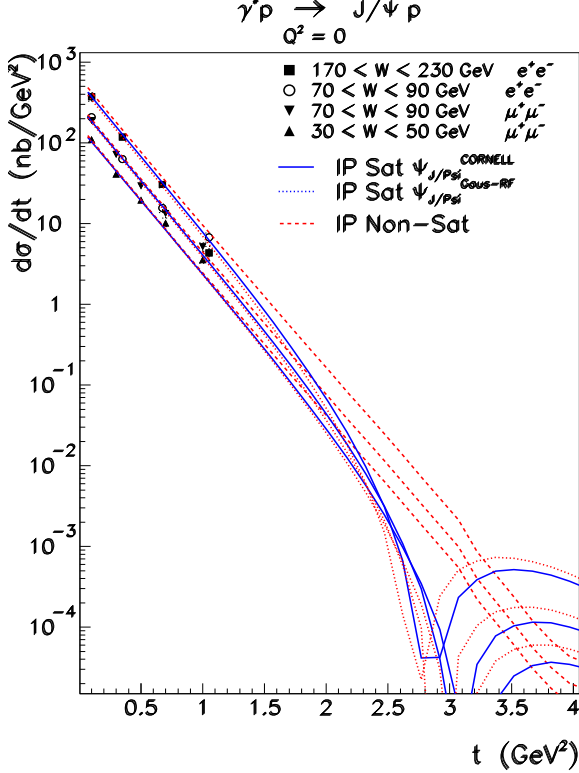


FIG. 16: A comparison of the measured diffractive J/ψ cross-sections [19] with the results of the IP Saturation model for two different J/ψ wave-functions. Also shown are the results of the non-saturated model evaluated with CORNELL wave-function.

cross section for various dipole sizes

$$\frac{d\sigma_{q\bar{q}}}{dt} = \left| \int d^2b e^{-ib \cdot \Delta} \frac{d\sigma_{q\bar{q}}}{d^2b} \right|^2. \quad (32)$$

For small r , the b dependence of the dipole cross section is essentially Gaussian and its Fourier transform is a pure exponential in t . For large r , due to saturation, the shape of the dipole cross section becomes more box-like, as seen in Fig. 2. The two dimensional Fourier transform of a box is proportional to the Bessel function J_1 which leads to dips in the t distribution. Although the distortions to the proton shape seen in Fig. 2 are small when displayed in coordinate space, they appear vividly after taking the Fourier transform and examining the t -distribution. For dipoles with $r \geq 3 \text{ GeV}^{-1}$ the t -distribution is substantially changed.

F. Saturation versus Non-Saturation

In order to isolate the effects of saturation we compared the results of the IP Saturation model with a model which is not unitarized. This model, denoted IP Non-Sat, re-

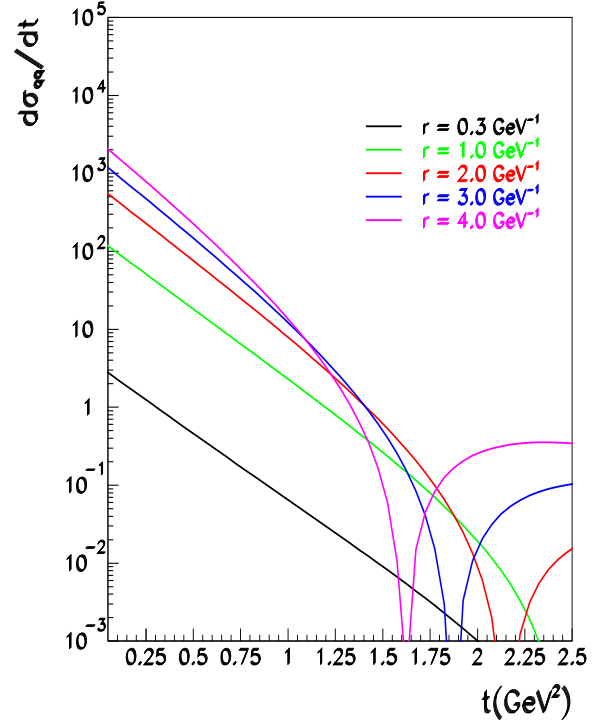


FIG. 17: The Fourier transform of the differential dipole $\frac{d\sigma_{q\bar{q}}}{d^2b}$ cross section for various dipole sizes.

places the dipole cross-section of Eq. 11 with the first term after expanding of the exponential

$$\frac{d\sigma_{q\bar{q}}}{d^2b} = \frac{\pi^2}{N_C} r^2 \alpha_s(\mu^2) x g(x, \mu^2) T(b). \quad (33)$$

The proton shape $T(b)$ was assumed to be the same as in the saturated case. The fit to the total cross section was repeated and a non-saturated gluon structure function was determined. The optimal fit was obtained for a higher quark mass than in the saturated case, $m_{u,d,s} = 150 \text{ MeV}$. This is expected since the dipole cross-section $\sigma_{q\bar{q}}$ grows faster with r than in the saturated case. The fit yields $A_g = 3.5$, $\lambda_g = -0.13$, $\mu_0^2 = 0.80$ and $\chi^2/N_{DF} = 0.8$. Naturally, the saturated and non-saturated dipole cross sections are very similar since they both fit the inclusive γ^*p cross-sections very well. Consequently, all observable cross-section which only are sensitive to the dipole cross-section integrated over impact parameter are indistinguishable. This was verified explicitly for the total diffractive J/ψ production. In particular, this agreement can be seen in Fig. 10 for the $\lambda_{tot}(Q^2)$ distribution. However, the gluon distributions are not the same as illustrated in Fig. 18 which compares the saturated and non-saturated models. For small dipole sizes the distributions are similar but they differ significantly as r becomes large.

The t -distribution provides additional insight into the dynamics of saturation in DIS. Figure 16 compares predictions for diffractive J/ψ production in the saturated and non-saturated modes. As discussed above saturation distorts the impact parameter distribution and leads unavoidably to diffractive dips in the t -distribution. Without saturation, as seen in Fig. 16, the exponential decrease continues to large t . Diffractive dips in the t distribution were clearly observed in elastic hadronic reactions [36]. In DIS processes at HERA the measured range of the t -distribution is too small for a dip to appear. In addition the HERA experiments have always measured elastic diffractive events with some small admixture of inelastic diffractive events. Even if inelastic events are a small fraction of the total, these events will dominate the t -distribution at large t since the inelastic t -distribution falls slowly [19, 36].

In the small t range, saturation slightly increases the slope parameter B of diffractive vector meson production at large W . Figure 19 compares the slope parameter B determined by the ZEUS experiment with model predictions. The observed increase of the slope B with W (called shrinkage) is slightly larger than the model prediction. This could be an indication that the shape $T(b)$ is somewhat dependent on x due to QCD evolution. Since considerably more data is available than was used in the present analysis we plan further study of the observed shrinkage.

Concluding we note that the t -distribution provides

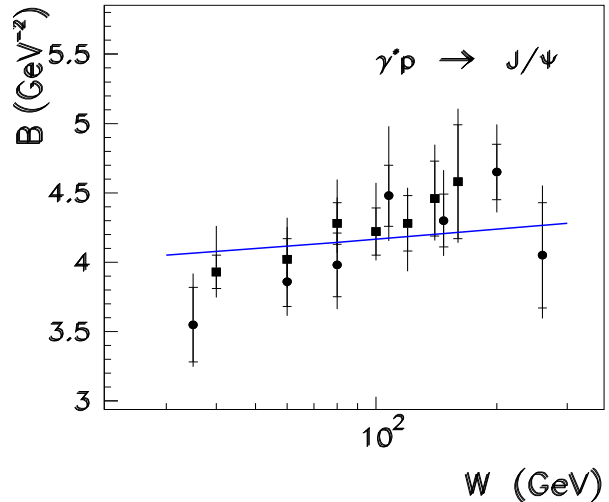


FIG. 19: The diffractive slope B measured by the ZEUS experiment as a function of W at $Q^2 = 0$. The solid line shows the prediction of the IP Saturation model.

precise information about the interplay of saturation and evolution phenomena. Therefore, it is crucially important to measure elastic vector meson production with a small systematic uncertainty over a wide range in t .

V. SATURATION SCALE Q_s^2

In the limit of high gluon density called the Color Glass Condensate (CGC)[4], the interaction probability in DIS becomes large. The probability of no interaction is measured by the square of the S-matrix element, $S^2(b)$. Normally, in high energy reactions the interaction probability is small, $S^2 \sim 1$. However, in the CGC limit this probability approaches unity, $S^2 \sim 0$. Figure 20 shows $S^2(b = 0)$ as a function of x for various dipole sizes. For small size dipoles the gluon structure function grows strongly with decreasing x and the S-matrix diminishes quickly. For large size dipoles, the gluon density does not grow and the S-matrix is small even at relatively large x .

To delineate the saturation region in the (x, r^2) plane we first define a density profile D

$$D(b, x, r^2) = \frac{2\pi^2}{N_C} \alpha_s(\mu^2(r^2)) xg(x, \mu^2(r^2)) T(b). \quad (34)$$

Then, the saturation radius r_S is defined as the dipole size for which proton consists of one interaction length

$$S^2 = \exp\left(-\frac{D(b, x, r_S^2) r_S^2}{2}\right) = e^{-1}. \quad (35)$$

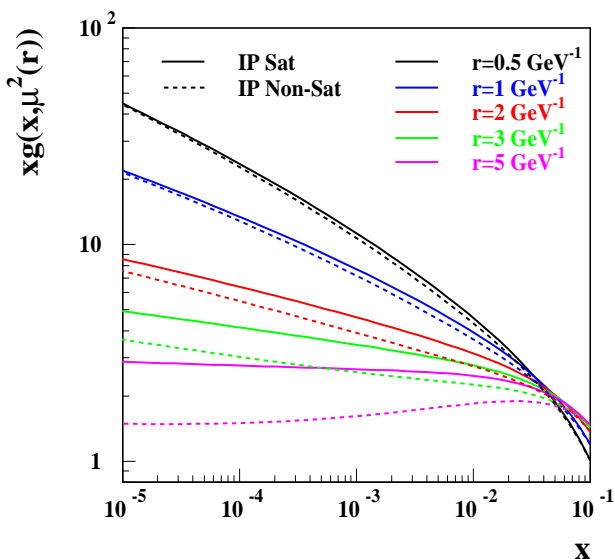


FIG. 18: A comparison of the gluon structure function in the IP Saturation and IP Non-Saturation models at various dipole sizes. The dipole size determines the evolution scale μ^2 .

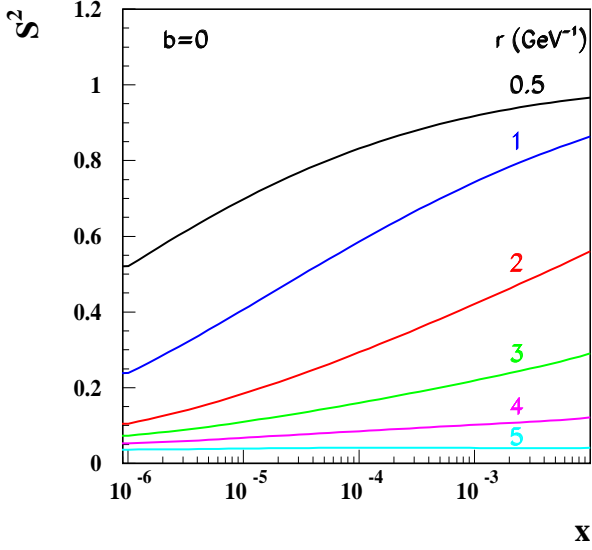


FIG. 20: The square of the S-matrix as a function of x for various dipole sizes.

This defines an implicit equation for r_S^2 which can be solved numerically. Now the saturation scale Q_S^2 is defined as the density profile D evaluated at the saturation radius

$$Q_S^2(b, x) = D(b, x, r_S^2) = \frac{2}{r_S^2}. \quad (36)$$

In the GBW model $S^2 = \exp(-r^2/2R_0^2)$ and we find $Q_S^2 = 1/R_0^2$ in accord with the original definition of the saturation scale. The saturation region is then defined by the condition that $r > r_S(b, x)$.

Figure 21 shows the saturation scale Q_S^2 as a function of $1/x$ in the central impact parameter region. We observe that the saturation scale is lower than the GBW value. This is primarily because the charm quark contribution to F_2 was neglected when the saturation scale was evaluated. Including the charm quark reduces the gluon density and the saturation scale.

We also calculated the S-Matrix element and determined the corresponding effective saturation scale for the non-saturated model. As seen in Fig. 21, the saturation scale is very similar for IP Saturated and IP Non-Saturated models. This is because the corresponding gluon structure functions are very similar for small size dipoles, as seen in Fig. 18. Therefore, our estimates of the saturation scale are only weakly model dependent.

Table II records the saturation radii and the percentage of the total γ^*p cross-section in the saturation region, $r > r_S$. At low Q^2 ($Q^2 = 0.4 \text{ GeV}^2$) the cross-section is dominated by dipoles which are larger than the saturation radius. As seen in Fig. 8, a fraction of these dipoles

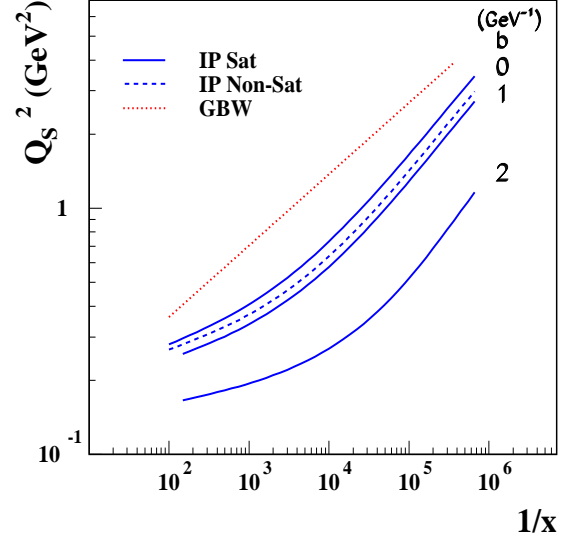


FIG. 21: The saturation scale as a function of x . The dashed curve shows the critical line ($S^2 = e^{-1}$) in the Non-Saturated model at $b = 0$.

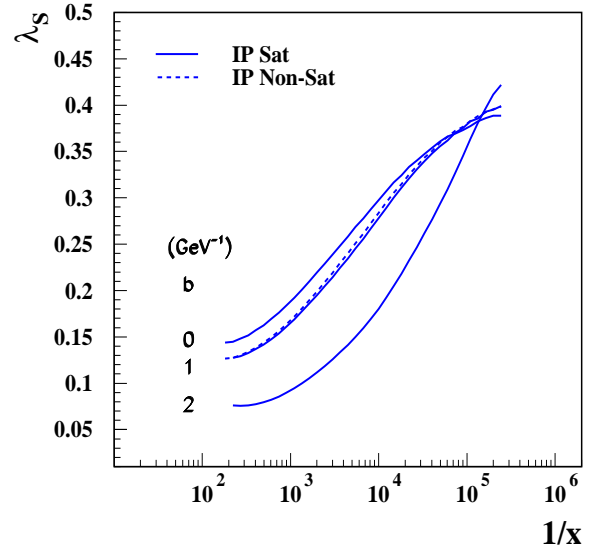


FIG. 22: The saturation exponent λ_S as a function of x and impact parameter. The dashed curve shows the exponent along the critical line ($S^2 = e^{-1}$) in the Non-Saturated model at $b = 0$.

may be considered perturbative since they are smaller than $r \lesssim 2 \text{ GeV}^{-1}$. In the large Q^2 region saturation is of secondary importance. The region $Q^2 \approx 4 \text{ GeV}^2$ is particularly interesting since a significant fraction of the dipoles are perturbative and are approximately the size of the saturation radius. BFKL and saturation dynamics are expected to influence observable cross sections in this kinematic domain.

It is also interesting to define the saturation exponent λ_S

$$\lambda_S = \frac{d \log(Q_S^2)}{d \log(1/x)}. \quad (37)$$

Figure 22 shows the saturation exponent λ_S as a function of $1/x$ for various impact parameters. The saturation exponent exhibits a sizable x dependence. It varies between $\lambda_S = 0.15$ at $x = 10^{-2}$ and $\lambda_S = 0.35$ at $x = 10^{-5}$ which should be contrasted with the constant GBW value, $\lambda_{GBW} = 0.29$. An analysis of BFKL evolution near the saturation boundary found that the exponent λ_S is nearly constant as a function of $\log(1/x)$ in the HERA kinematic window [37].

VI. NUCLEAR DEPENDENCE

Now that impact parameter distribution of the proton is taken into account, the dipole picture provides a framework for modeling nuclear phenomena in DIS. The distribution of nucleons in the nucleus $\rho_A(\vec{r})$ is parametrized according to the Woods-Saxon distribution [38]

$$\rho_A(\vec{r}) = \frac{N}{\exp\left(\frac{(r-R_A)}{\delta}\right) + 1}, \quad (38)$$

where A denotes the number of nucleons in the nucleus, $\delta = 0.54 \text{ fm}$, $R_A = (1.12 \text{ fm}) A^{1/3} - (0.86 \text{ fm}) A^{-1/3}$ and N is adjusted to normalize the distribution to one

$$\int d^3\vec{r} \rho_A(\vec{r}) = 1. \quad (39)$$

$b \text{ (GeV}^{-1}\text{)}$		0		1		2	
$Q^2 \text{ (GeV}^2\text{)}$	x	r_S	%	r_S	%	r_S	%
0.4	10^{-5}	1.1	72	1.3	68	2.0	52
0.4	10^{-4}	1.6	70	1.9	65	2.7	51
4.0	10^{-4}	1.6	33	1.9	25	2.7	17
4.0	10^{-3}	2.2	44	2.4	28	3.2	20
40.	10^{-3}	2.2	13	2.4	12	3.2	9
40.	10^{-2}	2.7	21	2.9	18	3.5	16

TABLE II: Table of saturation radii and of the percentages of the inclusive total γ^*p cross-section in the saturation region, $r > r_S$.

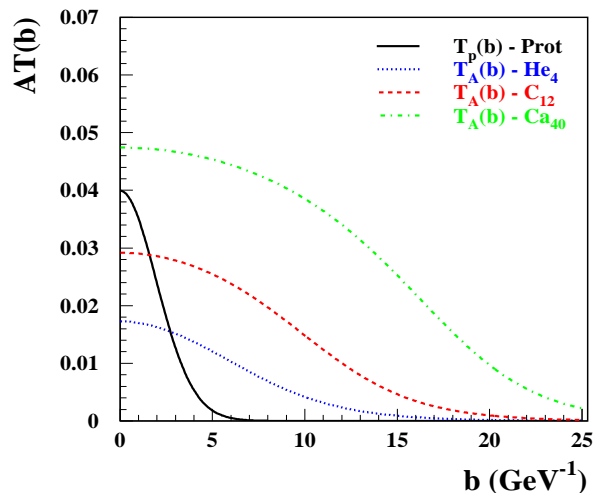


FIG. 23: The transverse density $AT_A(b)$ for several light nuclei compared to the proton transverse profile, $T_p(b)$.

The transverse distribution is defined as

$$T_A(\mathbf{b}) = \int_{-\infty}^{+\infty} dz \rho_A(\sqrt{\mathbf{b}^2 + z^2}). \quad (40)$$

Figure 23 compares the proton shape $T_p(b)$ with the transverse density $T_A(b)$ for several light nuclei.

For a first estimate of nuclear effects we assume that the gluons are distributed uniformly throughout the nucleus. This assumption is realized by replacing the proton shape in Eq. 16 by the integrated Woods-Saxon distribution $T_A(b)$ scaled by the number of nucleons,

$$\frac{d\sigma_{q\bar{q}}}{d^2b} = 2 \left[1 - \exp\left(-r^2 \frac{\pi^2}{2N_c} \alpha_s(\mu^2) x g(x, \mu^2) AT_A(b)\right) \right]. \quad (41)$$

This naive assumption, called the *smooth* nucleus assumption below, cannot be true since Fig. 23 shows that the center of the proton is on average more dense than the carbon nucleus. Nevertheless it is instructive to evaluate F_2^A/AF_2^p for this case and to compare it with NMC measurements of shadowing at small- x [39], see Fig. 24. The figure shows that the *smooth* nucleus assumption underestimates nuclear shadowing considerably as can be anticipated by comparing the densities in Fig. 23.

The proton profile $T_p(b)$ indicates that the gluons are distributed within individual nucleons with a radius of $\approx 0.5 \text{ fm}$. The nucleons are then distributed within the nucleus according to a Woods-Saxon distribution. Therefore the gluons form a *lumpy* distribution within the nucleus. To account for this correlation among the gluons we generalize the model in the following way. The probability of a given configuration of nucleons within the nucleus $\{(\mathbf{b}_1, z_1), (\mathbf{b}_2, z_2), \dots, (\mathbf{b}_A, z_A)\}$ is

$$P_{\{(\mathbf{b}_1, z_1), (\mathbf{b}_2, z_2), \dots, (\mathbf{b}_A, z_A)\}} = \prod_{i=1}^A \rho(\mathbf{b}_i, z_i). \quad (42)$$

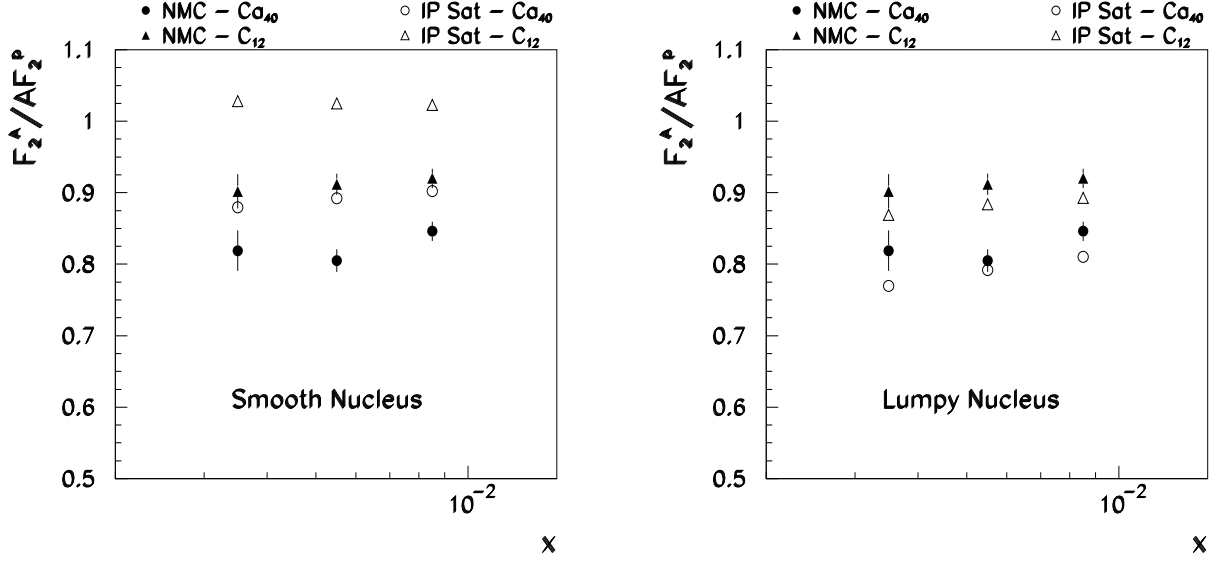


FIG. 24: Shadowing in DIS: a comparison of model predictions (open points) to data (full points) with the smooth and lumpy nucleus assumptions. The NMC measurements[39] were performed at $Q^2 = 0.74, 1.20, 1.70 \text{ GeV}^2$ for Carbon and at $Q^2 = 0.60, 0.94, 1.40 \text{ GeV}^2$ for Calcium (in order of increasing x values).

For a given configuration of nucleons the probability that the dipole scatters at impact parameter \mathbf{b} is

$$\left(\frac{d\sigma_{q\bar{q}}}{d^2b}\right)_{\{(\mathbf{b}_1, z_1), (\mathbf{b}_2, z_2), \dots, (\mathbf{b}_A, z_A)\}} = 2 \left[1 - \exp\left(-\frac{\pi^2}{2N_C} r^2 \alpha_s(\mu^2) x g(x, \mu^2) \sum_{i=1}^A T_p(\mathbf{b} - \mathbf{b}_i)\right) \right]. \quad (43)$$

Now we may average over all possible configurations of nucleons to determine the cross section

$$\frac{d\sigma_{q\bar{q}}}{d^2b} = \int d^2b_1 dz_1 \dots d^2b_A dz_A P_{\{(\mathbf{b}_1, z_1), (\mathbf{b}_2, z_2), \dots, (\mathbf{b}_A, z_A)\}} \left(\frac{d\sigma_{q\bar{q}}}{d^2b}\right)_{\{(\mathbf{b}_1, z_1), (\mathbf{b}_2, z_2), \dots, (\mathbf{b}_A, z_A)\}}. \quad (44)$$

Noticing that the integrals factorize we have

$$\frac{d\sigma_{q\bar{q}}}{d^2b} = 2[1 - (1 - I)^A] \quad (45)$$

$$I \equiv \int d^2b' T_A(\mathbf{b} + \mathbf{b}') \left[1 - \exp\left(-\frac{\pi^2}{2N_C} r^2 \alpha_s(\mu^2) x g(x, \mu^2) T_p(\mathbf{b}')\right) \right]. \quad (46)$$

To simplify this further, we notice that the integral over \mathbf{b}' is different from zero only over the size of the proton which is small compared to the nucleus even for the deuteron. Thus $T_A(\mathbf{b} + \mathbf{b}') \approx T_A(\mathbf{b})$. Using the definition of the total cross section of the $q\bar{q}$ pair on the proton $\sigma_{q\bar{q}}^p$ (Eq. 6 and 16) we have

$$\frac{d\sigma_{q\bar{q}}}{d^2b} = 2 \left[1 - \left(1 - \frac{T_A(\mathbf{b})}{2} \sigma_{q\bar{q}}^p\right)^A \right]. \quad (47)$$

Only if A is large and r is small do we recover the *smooth* nucleus formula of Eq. 41. Similar considerations were discussed in the context of setting up initial conditions for classical QCD simulations of nucleus-nucleus collisions [40]. Figure 24 shows that the *lumpy* nucleus model slightly overestimates the observed shadowing. However, good overall agreement with data clearly indicates that the IP Saturation model can be used to study of nuclear effects.

To estimate the saturation scale for heavy nuclei we follow the same procedure as for proton. We set the lumpy nucleus S-matrix element squared, $|S|^2 = (1 - \frac{T_A(b=0)}{2} \sigma_{q\bar{q}}^p)^{2A}$ equal to e^{-1} . This is an implicit equation for the saturation radius, r_S . Once r_S is determined numerically the saturation scale is determined from the relation, $Q_S^2 = 2/r_S^2$.

Figure 25 shows the saturation scale for various nuclei calculated in this fashion. It is interesting to observe that the saturation scale is not increasing like $A^{1/3}$. Rather, for Au the nuclear enhancement factor is only a factor of ≈ 2 at $x = 10^{-2}$ and ≈ 3 at $x = 10^{-4}$. When comparing the saturation scale to other estimates it is important to remember that this is the saturation scale for quarks. The saturation scale for gluons is $(Q_s^2)_g = \frac{N_c}{C_F} (Q_s^2)_q \approx 2.25 (Q_s^2)_q$ [41]. Thus for RHIC conditions with $x \approx 10^{-2}$, $(Q_s^2)_g$ is $\approx 1.3 \text{ GeV}^2$ which is slightly smaller than was estimated previously by analyzing RHIC multiplicity data [41, 42, 43, 44].

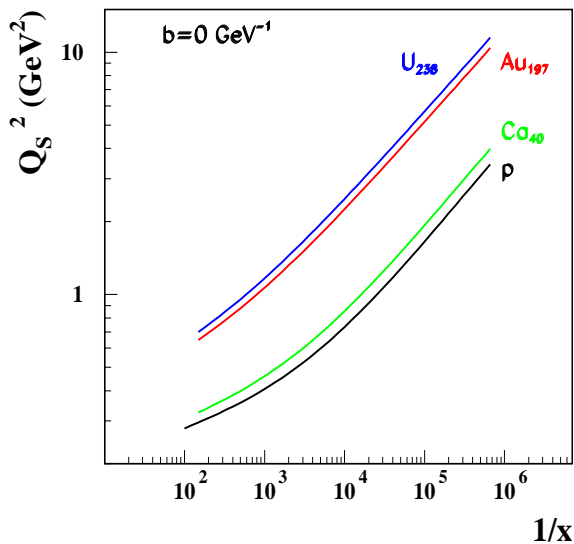


FIG. 25: The quark saturation scale $(Q_s^2)_q$ at $b = 0$ as a function of x for various nuclei. The gluon saturation scale is $(Q_s^2)_g = \frac{N_c}{C_F} (Q_s^2)_q \approx 2.25 (Q_s^2)_q$.

VII. SUMMARY

We developed an Impact Parameter dipole saturation model which describes HERA the total γ^*p cross section and differential diffractive J/ψ with high precision. The new feature of the model is an impact parameter dependent dipole cross-section which respects unitarity constraints. The impact parameter distribution is deter-

mined by measured J/ψ t -distributions to a large extent. For the functional form of the dipole cross-section we adopt the Glauber-Mueller formula [3] which can also be obtained within the McLerran-Venugopalan model [13].

The parameters of the dipole cross-section are determined from a fit to HERA data. The fit depends on the specific form of photon and the J/ψ wave function. At short distances, the photon wave-function is well known from QED. For the J/ψ wave-function we proposed several ansatzes and verified that the dipole cross-section was almost independent of these alternatives.

QCD evolution effects are taken into account by evolving the gluon structure function with the lowest order DGLAP equations. DGLAP evolution is essential in contrast to the GBW model.

In the dipole approach only the gluon structure function is modeled. All sea-quark contributions to F_2 are obtained from the photon wave-function and the subsequent dipole-gluon scattering. The validity of this approximation is corroborated by the excellent agreement between the predicted and observed open charm contribution to F_2 .

The impact parameter dependence of the dipole cross section determines the properties of the J/ψ total and diffractive cross-sections. The saturation ansatz for the dipole cross section predicts diffractive dips in the t distribution which are not necessarily predicted by an ansatz without saturation. For J/ψ production the diffractive dips appear in a region of t which is not covered by data but which is accessible to future measurements. In addition, the saturation ansatz predicts a slight increase of the diffractive slope B , which reflects a small increase in the proton size at small x . The change of the slope B with energy, called shrinkage, provides information about the interplay of saturation and evolution phenomena. Since shrinkage was observed for several vector-meson species and since considerably more data exists than was used in the present paper, further study of diffractive vector meson production and their t -distributions is warranted. We also point out that additional measurements of vector-meson production in an extended t -range would provide crucial information about the gluon density.

With an accurate determination of the S-matrix element we evaluated the saturation scale $Q_S^2(x)$ – the scale at which multiple collisions becomes important. The Q_S^2 determined in the model is approximately half of the GBW value and is only weakly dependent on the specific form of the dipole cross-section.

In the low Q^2 region up to $\sim 4 \text{ GeV}^2$, saturation dynamics contributes significantly to the observed cross-sections. The saturated state is at least partially perturbative since it is frequently initiated by small dipoles. Above $Q^2 \sim 10 \text{ GeV}^2$ saturation plays a secondary role. Dipoles are very small and although they are strong gluon emitters the gluon phase-space density remains small.

In order to isolate the effects of saturation, we also studied a dipole model which is not unitarized. This IP Non-Saturated model also obtained a good description of

the data. However, even with the non-saturated model the fit returned large gluon densities and unitarity corrections became important in the same region of x and Q^2 . Thus, the saturation ansatz is the more consistent approach.

The extension of the model to nuclei is fairly straightforward. We evaluated the nuclear cross-section with two different ansatzes for the distribution of gluons within the nucleus and compared the results to data on nuclear shadowing at low x . We found that the *lumpy* nucleus ansatz, in which gluons are distributed around the nucleons in a similar manner as around a free proton, leads to a good description of the data. We then used this ansatz to evaluate the saturation scale in heavy nuclei and found that Q_s^2 increases more slowly than $A^{1/3}$. Nevertheless, for Gold and Uranium Q_s^2 is enhanced by factor of ~ 2 when compared to the proton. For RHIC conditions the gluon saturation scale was found to be $Q_s^2 \approx 1.3 \text{ GeV}^2$, which is somewhat smaller than was estimated previously from RHIC multiplicity data [41].

The success of the model suggests that the saturated state known as the Color Glass Condensate plays an important role at HERA. Saturation is particularly important in the small x and low Q^2 region where the γ^*p total inclusive cross-section exhibits the same universal rate of growth as all known hadronic cross-sections. Revealing the Color Glass Condensate experimentally would represent a fundamental advance towards an understanding of the high energy limit of QCD.

VIII. ACKNOWLEDGMENT

We have profited from helpful discussions with many colleagues: A. Caldwell, J. Jalilian-Marian, D. Kharzeev, D. N. Triantafyllopoulos and R. Venugopalan. Our special thanks go to A. H. Mueller and L. McLerran. One of us (H.K.) thanks the Physics Department of Brookhaven National Laboratory and the Department of Physics of Columbia University for hospitality. Special thanks go to the Nevis Laboratories of Columbia University.

This work was partially supported by the National Science Foundation grant NSF PHY 00-98826 and by the U.S. Department of Energy grant DE-AC02-98CH10886.

APPENDIX A: THE J/ψ WAVE-FUNCTION

The discussion here closely follows [26] and uses some of the concepts of [25]. The light cone wave-function for J/ψ can be written as an expansion in the Fock space,

$$|V\rangle = \tilde{\psi}_{c\bar{c}} |c\bar{c}\rangle + \tilde{\psi}_{q\bar{q}g} |q\bar{q}g\rangle + \dots \quad (\text{A1})$$

Below we neglect higher Fock components in the wave-function and treat the meson as a predominantly a $c\bar{c}$ pair. Restoring indices, the J/ψ state is given by

$$|V^\lambda\rangle = \int \frac{d^2k dz}{16\pi^3} (\tilde{\psi}_V)_\lambda^{h\bar{h}}(\mathbf{k}, z) \frac{\delta_{ab}}{\sqrt{N_c}} |c^a(\mathbf{k}, z, h) \bar{c}^b(-\mathbf{k}, 1-z, \bar{h})\rangle \quad (\text{A2})$$

Here $\lambda = 0, \pm 1$ denotes the polarization of the vector meson, $h, \bar{h} = \pm$ denote the helicities of the c -quark and anti- c -quark respectively, and a, b are the color indices of the c -quark and anti- c -quark. Here and below we strictly adhere to the light-cone conventions of Ref. [24].

The J/ψ wave-function is modeled after the photon wave-function. The longitudinally polarized vector me-

son ($\lambda = 0$) is

$$(\tilde{\psi}_V)_0^{h\bar{h}}(k, z) = \frac{\delta_{h+\bar{h}-} + \delta_{h-\bar{h}+}}{\sqrt{2}} \tilde{\phi}_L(k, z), \quad (\text{A3})$$

while the two transverse polarizations ($\lambda = \pm 1$) are given by

$$\begin{aligned} (\tilde{\psi}_V)_{+1}^{h\bar{h}}(k, z) &= \left[+\frac{k}{m_c} e^{+i\varphi_k} (z\delta_{h+\bar{h}-} - (1-z)\delta_{h-\bar{h}+}) + \delta_{h+\bar{h}+} \right] \tilde{\phi}_T(k, z) \\ (\tilde{\psi}_V)_{-1}^{h\bar{h}}(k, z) &= \left[-\frac{k}{m_c} e^{-i\varphi_k} ((1-z)\delta_{h+\bar{h}-} - z\delta_{h-\bar{h}+}) + \delta_{h-\bar{h}-} \right] \tilde{\phi}_T(k, z), \end{aligned} \quad (\text{A4})$$

where $k e^{i\varphi_k} = k_x + ik_y$. Once the wave-function in momentum space is specified then Fourier transforms return

the wave-function in coordinate space

$$(\psi_V)_\lambda^{h\bar{h}}(r, z) = \int \frac{d^2k}{(2\pi)^2} e^{i\mathbf{k}\cdot\mathbf{r}} (\tilde{\psi}_V)_\lambda^{h\bar{h}}(k, z). \quad (\text{A5})$$

Note under Fourier transform $\pm k e^{\pm i\varphi_k} \tilde{\phi}(k, z)$ becomes $\mp i e^{\pm i\varphi_r} \partial_r \phi(r, z)$. The overlap with the photon wave-

function is then

$$\begin{aligned} (\gamma|V)_L &\equiv \sum_{h\bar{h}} (\psi_\gamma^*)_0^{h\bar{h}} (\psi_V)_{\bar{0}}^{h\bar{h}} = e_c \sqrt{2N_c} \left[2z(1-z)Q \frac{K_0(\epsilon r)}{2\pi} \phi_L \right] \\ (\gamma|V)_T &\equiv \frac{1}{2} \sum_{\lambda=\pm 1} (\psi_\gamma^*)_\lambda^{h\bar{h}} (\psi_V)_\lambda^{h\bar{h}} = e_c \sqrt{2N_c} \left[(z^2 + (1-z)^2) \left(-\frac{1}{m_c} \frac{\partial \phi_T}{\partial r} \right) \frac{\epsilon K_1(\epsilon r)}{2\pi} + \phi_T m_c \frac{K_0(\epsilon r)}{2\pi} \right]. \end{aligned} \quad (\text{A6})$$

Two inputs are used to constrain the wave-function $\tilde{\phi}_{L,T}$. The first input is the normalization of the wave-function, $\langle V^{\lambda'} | V^\lambda \rangle = (2\pi)^3 2p^+ \delta(p'^+ - p^+) \delta^2(\mathbf{p}' - \mathbf{p}) \delta^{\lambda'\lambda}$. This leads to the requirement that

$$1 = \int \frac{d^2 k dz}{16\pi^3} \sum_{h\bar{h}} \left| (\tilde{\psi}_V)_\lambda^{h\bar{h}}(k, z) \right|^2, \quad (\text{A7})$$

or

$$1 = \int \frac{d^2 k dz}{16\pi^3} \left| \tilde{\phi}_L(k, z) \right|^2 \quad (\text{A8})$$

for $\tilde{\phi}_L$ and

$$1 = \int \frac{d^2 k dz}{16\pi^3} \left\{ (z^2 + (1-z)^2) \frac{k^2}{m_c^2} + 1 \right\} \left| \tilde{\phi}_T(k, z) \right|^2 \quad (\text{A9})$$

for $\tilde{\phi}_T$. Note that the formula (B19b) in [26] is incorrect by a factor of two for the transverse wave-function. The second input is the leptonic decay width of the vector meson. The decay width of the meson is given by

$$\Gamma_V = \frac{4\pi\alpha_{em}^2 f_V^2}{3 M_V}, \quad (\text{A10})$$

where f_V is given by

$$e M_V f_V \epsilon_\lambda^\mu = \langle 0 | J_{em}^\mu | V^\lambda \rangle. \quad (\text{A11})$$

In this formula $\epsilon_\lambda^\mu = (\epsilon^+, \epsilon^-, \epsilon_x, \epsilon_y)$ is the polarization vector of the meson and e is the charge of the positron. $\epsilon_{\pm 1}^\mu = 1/\sqrt{2}(0, 0, 1, \pm i)$ for transversely polarized mesons and $\epsilon_0^\mu = (\frac{p^+}{M_V}, -\frac{M_V}{p^+}, 0, 0)$ for the longitudinally polarized mesons. Evaluating this matrix element in light cone perturbation with the conventions of [24] gives

$$\begin{aligned} f_V &= \hat{e}_c \sqrt{2N_c} 2 \int \frac{d^2 k dz}{16\pi^3} \tilde{\phi}_L(k, z) \\ f_V &= \hat{e}_c \sqrt{2N_c} \frac{m_c}{M_V} \int \frac{d^2 k dz}{16\pi^3} \left\{ (z^2 + (1-z)^2) \frac{k^2}{m_c^2} + 1 \right\} \frac{\tilde{\phi}_T(k, z)}{z(1-z)}, \end{aligned} \quad (\text{A12})$$

where $\hat{e}_c = +\frac{2}{3}$ (in contrast to $e_c = \sqrt{4\pi\alpha_{em}}\hat{e}_c$) is the charge in units of the positron charge.

To go further, we must specify the form of the wave-function. We have studied three model wave-functions, GAUS-RF, CORNELL, and GAUS-LC. Two of the models (GAUS-RF and CORNELL) are motivated by the expected long distance behavior of the wave-function. One of models (GAUS-LC) is motivated by the expected short distance behavior of the wave-function.

For large distances, and for truly heavy vector mesons, the non-relativistic wave-function should give a good description of the light cone wave-function. To make the correspondence between the light cone and non-

relativistic wave-functions we repeat the discussion in Ref. [25]. In the non relativistic limit, terms proportional to $\left(\frac{k_\perp}{m_c}\right)^2$ can be dropped and the the normalization condition Eq. A7 is identical for the longitudinal and transverse wave-functions. Simple kinematic relations give the invariant mass of the the quark antiquark pair $M_V^2 = (p_1 + p_2)^2 = \frac{m_c^2 + k_\perp^2}{z(1-z)}$. This relation assumes that the quark and antiquark are on shell, which is true for non-relativistic quarks to order $\sim \left(\frac{k_\perp}{m_c}\right)^2$. In the rest frame of the meson (where the quarks have momentum \vec{p} and $-\vec{p}$) the invariant mass is $(p_1 + p_2)^2 = 4(p^2 + m_c^2)$.

Comparing these terms gives the identification

$$p^2 \rightarrow \frac{k_t^2 + (2z-1)^2 m_c^2}{4z(1-z)} \quad (\text{A13})$$

$$d^3p \rightarrow \frac{\sqrt{k_t^2 + m_c^2}}{4[z(1-z)]^{3/2}} d^2k_t dz. \quad (\text{A14})$$

Requiring probability conservation per unit phase space

$$\frac{d^3p}{(2\pi)^3} |\tilde{\psi}_{NR}(p)|^2 = \frac{d^2k_t dz}{16\pi^3} |\tilde{\phi}_{L,T}(k_t, z)|^2, \quad (\text{A15})$$

leads to the identification

$$\tilde{\phi}_{L,T}(k_t, z) = N_{L,T} \left(\frac{k_t^2 + m_c^2}{4z^3(1-z)^3} \right)^{\frac{1}{4}} \tilde{\psi}_{NR} \left(p = \sqrt{\frac{k_t^2 + (2z-1)^2 m_c^2}{4z(1-z)}} \right). \quad (\text{A16})$$

Here $\tilde{\psi}_{NR}(p)$ is the non-relativistic wave-function in momentum space

$$\psi_{NR}(\vec{x}) = \int \frac{d^3p}{(2\pi)^3} e^{i\vec{p}\cdot\vec{x}} \tilde{\psi}_{NR}(\vec{p}). \quad (\text{A17})$$

For the two long distance models (GAUS-RF and CORNELL) $\tilde{\psi}_{NR}(p)$ is specified. Then with the form of $\tilde{\phi}_{L,T}$ specified, the non-relativistic motivation for the light cone wave-function is abandoned and $N_{L,T}$ are constants adjusted to satisfy the normalization and decay conditions (Eqs. A7 and A12) including the terms proportional to $(k_t/m_c)^2$. Terms proportional to $(k_t/m_c)^2$ mock up relativistic effects and constitute $\approx 25\%$ of the total elastic diffractive cross section. For the short distance model (GAUS-LC) $\tilde{\phi}_{L,T}$ is specified directly. For the numerical results quoted below we take $M_V = 3.096$ GeV and $m_c = 1.3$ GeV.

GAUS-RF. In this model we take

$$\tilde{\psi}_{NR}(p) = N_{L,T} \exp\left(-\frac{p^2}{\omega_{L,T}^2}\right), \quad (\text{A18})$$

where $\omega_{L,T}$ and $N_{L,T}$ are adjusted to satisfy Eq. A12 for the decay width and Eq. A7 for the norm. These parameters are $N_L = 1.74$ GeV $^{-3/2}$, $\omega_L = 0.66$ GeV and $N_T = 1.86$ GeV $^{-3/2}$ and $\omega_T = 0.61$ GeV.

CORNELL. In this model we take the form of $\tilde{\psi}_{NR}(p)$ from the wave-function of a non-relativistic potential model of J/ψ . Using a shooting method [45] we solve the radial Schrödinger equation for the Cornell potential to find $\psi_{NR}(\vec{x})$. The parameters of the potential are taken from Ref. [27]. Note, the constituent quark mass of the potential model ($m_c = 1.8$ GeV) differs from the current quark mass ($m_c = 1.3$ GeV) in Eqs. A3, A4, A16 for the the light cone wave-function. In this model the decay condition Eq. A12 is not satisfied.

GAUS-LC. We now turn to the short distance model GAUS-LC. At short distances the light cone vector meson wave-function is proportional to $\propto z(1-z)$ [24, 25]. This motivates the following ansatz for the wave-function

$$\tilde{\phi}_{L,T}(r, z) = N_{L,T} z(1-z) \exp\left(-\frac{k^2}{\omega_{L,T}^2}\right) \quad (\text{A19})$$

$N_{L,T}$ and $\omega_{L,T}$ are adjusted to reproduce the normalization condition and the decay width. For J/ψ we find: $N_L = 1.21$ GeV $^{-1}$, $\omega_L = 0.80$ GeV and $N_T = 1.63$ GeV $^{-1}$ and $\omega_T = 0.58$ GeV.

With the wave-function $\tilde{\phi}_{L,T}(k, z)$ specified the wave-function $\phi_{L,T}(r, z)$ and its derivative $\partial_r \phi(r, z)$. are found taking Fourier transforms. The final overlap between the photon and vector meson wave-function is given by Eq. A6.

-
- [1] K.Golec-Biernat, M.Wuesthoff, Phys. Rev. **D59**, 014017 (1999); Phys. Rev. **D60**, 114023 (1999).
 [2] J. Bartels, K.Golec-Biernat, H. Kowalski, Phys. Rev. **D66**, 014001 (2002).
 [3] A.H. Mueller, Nucl. Phys. **B335**, 115 (1990).
 [4] For reviews and references see: E. Iancu, A. Leonidov, L. McLerran, hep-ph/0202270; A.H. Mueller, hep-ph/0111244; in *QCD Perspectives on Hot and Dense Matter*, E. Iancu and J. P. Blaizot eds., Kluwer Academic Publishers (2002).
 [5] S. Munier, A.M. Staśto, A.H. Mueller, Nuclear Physics **B603**, 427 (2001).

- [6] E. Gotsman, E. Levin, M. Lublinsky, U. Maor, Eur. Phys. J. **C27**, 411 (2003); E. Levin, M. Lublinsky, Phys. Lett. **B521**, 233 (2001); E. Levin, M. Lublinsky, Nucl. Phys. **A712**, 95 (2002).
 [7] J. Bartels et al., hep-ph/0304166.
 [8] N.N. Nikolaev, B.G. Zakharov, Z. Phys. **C49**, 607 (1991); N.N. Nikolaev, B.G. Zakharov, Z. Phys. **C53**, 331 (1991); N.N. Nikolaev, B.G. Zakharov, Z. Phys. **C64**, 651 (1994); N.N. Nikolaev, B.G. Zakharov, JETP **78**, 598 (1994).
 [9] A.H. Mueller, Nucl. Phys. **B415**, 373 (1994); A.H. Mueller, B. Patel, Nucl. Phys. **B425**, 471 (1994); A.H. Mueller, Nucl. Phys. **B437**, 107 (1995).

- [10] J.D. Bjorken, J.B. Kogut and D.E. Soper, Phys. Rev. **D3**, 1382 (1970).
- [11] S.J. Brodsky et al., Phys. Rev. **D50**, 3134 (1994).
- [12] L. Frankfurt, A. Radyushkin, and M. Strikman, Phys. Rev. **D55**, 98 (1997).
- [13] L. McLerran, R. Venugopalan, Phys. Rev. **D49**, 2233 (1994); Phys. Rev. **D49**, 3352 (1994); Phys. Rev. **D50**, 2225 (1994).
- [14] A.I. Shoshi, F.D. Steffen and H.J. Pirner, Nucl. Phys. **A709**, 131 (2002).
- [15] I. Balitsky, Nucl. Phys. **B463**, 99 (1996).
- [16] Yu.V. Kovchegov, Phys. Rev. **D60**, 034008 (1999); Phys. Rev. **D61**, 074018 (2000).
- [17] H1 Collab., S. Aid et al., Nucl. Phys. **B463**, 3 (1996); ZEUS Collab., J. Breitweg et al., Eur. Phys. J. **C2**, 247 (1998); ZEUS Collab., M. Derrick et al., Z. Phys. **C73**, 1,73 (1996); ZEUS Collab., M. Derrick et al., Phys. Lett. **B377**, 259 (1996); H1 Collab., C. Adloff et al., Phys. Lett. **B483**, 23 (2000); H1 Collab., C. Adloff et al., Eur. Phys. J. **C13**, 371 (2000); ZEUS Collab., J. Breitweg et al., accepted by Phys. Lett. B-PLB 16283; H1 Collab., C. Adloff et al., Phys. Lett. **B483**, 360 (2000); H1 Collab., C. Adloff et al., Eur. Phys. J. **C10**, 373 (1999); for a review of data see: B. Mellado, <http://arXiv.org/abs/hep-ex/0011050>.
- [18] H1 Collab., C. Adloff et al., Eur. Phys. J. **C10**, 373 (1999).
- [19] ZEUS Collab., S. Chekanov et al., Eur. Phys. J. **C24**, 345 (2002).
- [20] Wu-Ki Tung, Stefan Kretzer, Carl Schmidt, J. Phys. **G28**, 983 (2002).
- [21] M. Glück, E. Reya and A. Vogt, Eur. Phys. J. **C5**, 461 (1998).
- [22] J. Bartels, H. Kowalski, Eur. Phys. J. **C19**, 693 (2001).
- [23] A. Caldwell, M.S. Soares, Nucl. Phys. **A696**, 125 (2001).
- [24] S. Brodsky, P. Lepage, Phys. Rev. **D9**, 2157 (1980).
- [25] L. Frankfurt W. Koepf, and M. Strikman, Phys. Rev. **D54**, 3194 (1996); Phys. Rev. **D57**, 512 (1998).
- [26] H.G. Dosch, G. Kulzinger, H.J. Pirner, Eur. Phys. J. **C7**, 73 (1999).
- [27] E. Eichten, K. Gottfried, T. Kinoshita, K.D. Lane and T.-M. Yan, Phys. Rev. **D17**, 3090 (1978).
- [28] W. Buchmüller and S.-H. H. Tye, Phys. Rev. **D24**, 132 (1981).
- [29] E. Eichten and C. Quigg, Phys. Rev. **D52**, 1726 (1995).
- [30] ZEUS Collab., J. Breitweg et al., Phys. Lett. **B487**, 53 (2000); H1 Collab., C. Adloff et al., Eur. Phys. J. **C21**, 3 (2001); ZEUS Collab., S. Chekanov et al., Eur. Phys. J. **C21**, 443 (2001).
- [31] A. Donnachie, P.V. Landshoff, Nucl. Phys. **B244**, 322 (1984).
- [32] ZEUS Collab., J. Breitweg et al., Eur. Phys. J. **C12**, 35 (2000).
- [33] H1 Collab., C. Adloff et al., Phys. Lett. **B528**, 199 (2002).
- [34] A.D. Martin, R.G. Roberts, W.J. Stirling and R.S. Thorne Eur. Phys. J. **C4**, 463 (1998).
- [35] R. Thorne, HERA III Workshop, Munich (2002); J. Bartels, HERA III Workshop, Munich (2002); wwwhera-b.mppmu.mpg.de/hera3/Presentations.html.
- [36] K. Goulianos, Physics Reports **101**, 169 (1983).
- [37] D. N. Triantafyllopoulos, Nucl. Phys. **B648**, 293 (2003).
- [38] A. Bohr and B.R. Mottelson, *Nuclear Structure*, Benjamin, New York 1969.
- [39] NMC Collab. P Amaudruz et al., Nucl. Phys. **B441**, 3 (1995).
- [40] A. Krasnitz, Y. Nara, R. Venugopalan, Nucl. Phys. **A717**, 2003 (268).
- [41] A. Mueller, Quark-Matter 2002, hep-ph/0208278.
- [42] D. Kharzeev and M. Nardi, Phys. Lett. **B507**, 121 (2001).
- [43] A. Krasnitz, Y. Nara, R. Venugopalan, Phys. Rev. Lett. **87**, 192302-1 (2001).
- [44] D. Kharzeev and E. Levin, Phys. Lett. **B523**, 79 (2001).
- [45] W. Press, B. Flannery, S. Teukolsky, W. Vetterling, *Numerical Recipes: The Art of Scientific Computing*, Cambridge University Press, (1992).
- [46] z denotes the longitudinal direction and not the quark light cone momentum fraction in this paragraph.